EXPERIMENTAL INVESTIGATION OF A NOVEL ROTARY WAVE ENERGY CONVERTER UNDER REGULAR WAVE CONDITIONS IN A CONTROLLED WAVE FLUME

A THESIS SUBMITTED TO
THE GRADUATE SCHOOL OF NATURAL AND APPLIED SCIENCES
OF
ANKARA UNIVERSITY

by

Abdalla ALKHALEDI

IN PARTIAL FULFILMENT OF THE REQUIREMENTS
FOR THE DEGREE OF
MASTER OF SCIENCE IN
ENERGY ENGINEERING

ANKARA
2025

ABSTRACT

Master Thesis

EXPERIMENTAL INVESTIGATION OF A NOVEL ROTARY WAVE ENERGY CONVERTER UNDER REGULAR WAVE CONDITIONS IN A CONTROLLED WAVE FLUME

Abdalla ALKHALEDI

Ankara University
Graduate School of Natural and Applied Sciences
Department of Energy Engineering

Supervisor: Asst. Prof. Dr. Özgür SELİMOĞLU

This study investigated the wave energy conversion performance of a novel rotary wave energy converter (WEC) prototype designed to overcome some of the limitations of traditional drag- and lift-based converters by combining their simplicity and efficiency. The system utilized hinged, symmetrical hydrofoils to harness wave-induced torque and was tested in a controlled wave flume under regular shallow and intermediate water wave conditions. Experiments systematically varied wave heights, wave periods, submergence levels, and rotational speeds to identify optimal operating conditions. The converter achieved a maximum efficiency of 8.31% under a wave height of 10 cm, a wave period of 2 s, a submergence level of -10 cm below the free surface, and a rotational speed set at 50% of the angular wave frequency. Efficiency was calculated using fifth-order nonlinear wave models and validated against a rotor-free numerical simulation. A deep learning model was developed to analyze the operational parameters relative to efficiency, and the wave period was identified as the most influential factor. By demonstrating the technical viability of the proposed converter, this study established a foundation for optimizing design and improving scalability for real-world applications. It contributes to advancing renewable energy technologies, offering a cost-effective and sustainable pathway toward harnessing ocean energy.

March 2025, 89 Pages

Key Words: Renewable Energy, Wave Energy Conversion, Rotary Wave Energy Converter, Experimental Wave Flume, Water Wave Theory

ÖZET

Yüksek Lisans Tezi

DÜZENLİ DALGA KOŞULLARINDA KONTROLLÜ DALGA KANALINDA YENİ BİR DÖNER TİP DALGA ENERJİ DÖNÜŞTÜRÜCÜSÜNÜN DENEYSEL İNCELENMESİ

Abdalla ALKHALEDI

Ankara Üniversitesi
Fen Bilimleri Enstitüsü
Enerji Mühendisliği Anabilim Dalı

Danışman: Dr. Öğr. Üyesi Özgür SELİMOĞLU

Bu çalışmada, geleneksel sürüklenme ve kaldırma temelli enerji dönüştürücülerinin bazı sınırlamalarını aşmak için tasarlanan, basitliklerini ve verimliliklerini birleştiren yeni bir döner tip dalga enerji dönüştürücüsü (WEC) prototipinin dalga enerjisi dönüşüm performansı incelenmiştir. Sistem, dalga kaynaklı torku yakalamak için menteşeli, simetrik hidrofoiller kullanmıştır ve düzenli sığ ve orta su derinliğindeki dalga koşulları altında kontrollü bir dalga kanalında test edilmiştir. Deneylerde, optimum çalışma koşullarını belirlemek amacıyla dalga yükseklikleri, dalga periyotları, daldırma seviyeleri ve dönme hızları sistematik olarak değiştirilmiştir. Dönüştürücü, 10 cm dalga yüksekliği, 2 s dalga periyodu, serbest yüzeyin 10 cm altındaki daldırma seviyesi ve dalga frekansının %50'sine ayarlanmış bir dönme hızı altında maksimum %8,31 verimlilik sağlamıştır. Verimlilik, beşinci dereceden doğrusal olmayan dalga modelleri kullanılarak hesaplanmış ve rotorsuz bir sayısal dalga kanal modeli ile doğrulanmıştır. Çalışma, verimlilikle ilgili operasyonel parametreleri analiz etmek için geliştirilen bir derin öğrenme modeliyle desteklenmiş ve dalga periyodunun en etkili faktör olduğu belirlenmiştir. Bu çalışma, önerilen dönüştürücünün teknik uygulanabilirliğini göstererek tasarım optimizasyonu ve gerçek dünya uygulamaları için ölçeklenebilirliği artırmaya yönelik bir temel oluşturmuştur. Çalışma, yenilenebilir enerji teknolojilerini ilerletmeye katkı sağlayarak okyanus enerjisinden yararlanmaya yönelik maliyet etkin ve sürdürülebilir bir yol sunmaktadır.

Mart 2025, 89 Sayfa

Anahtar Kelimeler: Yenilenebilir Enerji, Dalga Enerjisi Dönüşümü, Döner Tip Dalga Enerji Dönüştürücüsü, Deneysel Dalga Kanalı, Su Dalgası Teorisi

FOREWORD AND ACKNOWLEDGEMENTS

I wish to express my deepest gratitude to my supervisor, Asst. Prof. Dr. Özgür SELİMOĞLU, for his exceptional guidance, encouragement, and support throughout the course of this study. His extensive knowledge and expertise have been a constant source of inspiration, significantly enriching both my academic and practical understanding. His insightful advice has played a pivotal role in the successful completion of this work.

I would also like to extend my heartfelt thanks to my friends and colleagues for their meaningful contributions and unwavering support during this journey. Their encouragement, collaboration, and shared insights have not only helped me navigate challenges but also fostered a spirit of teamwork that I deeply value.

Additionally, I am profoundly thankful to my family for their unconditional love, patience, and encouragement. Their unwavering belief in me has been the foundation of my strength and perseverance. I am especially indebted to my dear parents, whose sacrifices, faith, and endless support have made this journey possible. It is to them that I dedicate this thesis with immense gratitude and love.

Finally, to everyone who has supported, encouraged, or contributed to this journey, whether directly or indirectly, I sincerely thank you. Your kindness, generosity, and belief in me have been truly invaluable.

Abdalla ALKHALEDI
Ankara, March 2025

TABLE OF CONTENTS

SYMBOLS AND ABBREVIATIONS

a_1	Model coefficient
B_i	Coefficients of the Stokes wave theory
C_i	Coefficients of the Stokes wave theory
C_1	Linear (temporal) damping resistance
C_2	Quadratic (special) damping resistance
c_{num}	Numerically calculated wave speed
c	Wave speed
cn	Elliptic cosine function
D_i	Coefficients of the Stokes wave theory
D_ω	Cross-diffusion effect term
d	Mean water depth
d_n	Coefficients of Hunt's wavelength approximation
E_i	Coefficients of the Stokes wave theory
E	Linear wave energy density
E_k	Kinetic energy density
E(m)	Complete elliptic integral of the second kind
E_p	Potential energy density
e	Elliptic integrals ratio
F	Mean energy flux
F_2	Blending function
F_{Froude}	Froude number
f_p	Volume fraction of the air phase
f_q	Volume fraction of the water
G_b	Buoyancy effect term
$G_{\omega b}$	Buoyancy effect term
g	Gravitational acceleration
H	Wave height
H_{max}	Theoretical maximum unbroken wave height
h	Depth under the wave trough
I	Mean wave momentum
k	Wave number / Turbulent kinetic energy
K(m)	Type 1 complete elliptic integral
m	Elliptic modulus
$\dot{m}_{pq}$	Interfacial flow rate from primary to secondary
$\dot{m}_{qp}$	Interfacial flow rate from secondary to primary
N_{rotor}	Rotor's rotational speed
N_{motor}	Motor's rotational speed
N_{sensor}	Sensor's rotational speed
P_{avg}	Mean experimental wave power
P_{th}	Theoretical wave power
P	Pressure field
Q	Volumetric flow rate per unit width
R	Bernoulli's constant
S	Strain rate magnitude

S_{ij}	Time-averaged strain tensor
S_{sink}	Damping sink term
T	Wave period
T_{kin}	Mean kinetic energy
t	Elapsed time
t_1	Time at monitor 1
t_2	Time at monitor 2
U	Horizontal velocity component in a non-inertial frame of reference
$\overline{U}$	Mean horizontal velocity component at a given elevation
u_i	Velocity field
u	Horizontal velocity in an inertial frame
u'	Fluctuating velocity term
$\bar{u}$	Mean horizontal velocity
$\bar{u}_1$	Mean current
$\bar{u}_2$	Mean mass transport velocity
$\bar{u}_b$	Mean horizontal velocity component at the bed
U_p	Goda's universal wave parameter
U_{Ursel}	Ursel number
V	Vertical velocity component in a non-inertial frame
V_{pot}	Mean potential energy
v_x	Horizontal velocity component
v_y	Vertical velocity component
v	Vertical velocity component in an inertial frame
x	Horizontal position in an inertial frame
X	Horizontal position in a non-inertial frame
x_i	Horizontal position in the flow direction
x_s	Start point of damping region
x_e	End point of damping region
$\hat{x}$	Argument of the elliptic cosine function
y	Vertical position coordinate in an inertial frame
Y	Vertical position coordinate in a non-inertial frame
y_i	Vertical position perpendicular to wave propagation
y_b	Bottom floor of the flume
y_{fs}	Free surface level
Y_k	Dissipation effect term
Y_ω	Dissipation effect term
α	Shallowness parameter / Turbulence model constant
δ	Kronecker delta operator
ε	Wave steepness
η	Free surface elevation / Efficiency
λ	Wavelength
μ	Dynamic viscosity
μ_t	Turbulent (eddy) viscosity
ν	Turbulent kinematic viscosity
ρ	Water density
σ_k	Turbulent Prandtl number
σ_ω	Turbulent Prandtl number
$\tau_{avg\text{-}net}$	Experimental average net torque

ψ	Stream function
ω	Angular wave frequency / Specific dissipation rate

Abbreviations

AYGM	Altyapı Yatırımları Genel Müdürlüğü (Directorate General of Infrastructure Investments)
CAD	Computer-aided design
CFD	Computational fluid dynamics
EWF	Experimental wave flume
FVM	Finite volume method
HRIC	High-resolution interface capturing
IPLS	Initial phase-locked strategy
MAE	Mean absolute error
MAPE	Mean absolute percent error
MSE	Mean square error
NWF	Numerical wave flume
OB	Oscillating bodies
OD	Overtopping devices
OWC	Oscillating water column
PISO	Pressure-implicit with splitting of operators
PLS	Phase-locked strategy
PRESTO!	Pressure staggering option
PTO	Power take-off
PUS	Phase unlocked strategy
RANS	Reynolds-averaged Navier-Stokes
RMSE	Root mean square error
SHAP	Shapley additive explanations
SST	Shear stress transport
VOF	Volume of fluid
WEC	Wave energy converter

LIST OF FIGURES

LIST OF TABLES

1. INTRODUCTION

1.1 Background and Problem Description

As the global reliance on fossil fuels continues to diminish due to climate awareness, the demand for sustainable energy resources has increased at an unprecedented rate. In that regard, wave energy has been attracting growing attention among the available renewable alternatives. In 2020, the potential capacity of wave energy was reported at 29500 TWh, but with an active capacity of only 2.31 MW, while the global energy demand was reported at 25000 TWh. Furthermore, wave energy is much more abundant and contains a higher energy density than other renewable resources, making it more reliable. For example, typical energy densities of wind and solar resources are around 0.4 to 0.6 and 0.1 to 0.2 kW/m^2, respectively, while the energy density of water waves is between 2 to 3 kW/m^2. Moreover, wave energy has a good resource-to-demand balance, since 37% of people live within 90 km from the coast. Despite its potential, wave energy is still relatively immature, and further research and investments are required for large-scale commercialization (López et al., 2013; IRENA, 2020; Jin et al., 2022).

Wave energy can be harnessed using wave energy converters, or WECs for short. These devices convert the energy of the waves into useful power. WECs have been a research topic since the early 1970s and still constitute a growing research interest in terms of technical and economic feasibility. WECs are often classified based on their wave interaction, location with respect to shore, and drive mechanism. In general, oscillating water column (OWC) devices, oscillating body (OB) devices, and overtopping (OD) devices are the most commonly encountered categories of converters (López-Ruiz et al., 2016; IRENA, 2020; Qiao et al., 2020; Depalo et al., 2021).

Oscillating water column (OWC) devices consist of a partially submerged air chamber within which the water level varies in response to incident waves, forcing the air in and out of the chamber over a turbine. They are simple and have low environmental impacts. Additionally, OWCs can be stand-alone devices or integrated into coastal

structures. Notable examples can be found in Portugal, Scotland, and Australia, as shown in Figure 1.1, where these locations were chosen due to their high wave energy potential and favorable environmental conditions, with rated capacities ranging from 400 to 500 kW (Falcão, 2000; Heath et al., 2000; Alcorn et al., 2005; IRENA, 2020).

(a) Pico Island, Portugal (400 kW)

(b) Islay, Scotland (500 kW)

(c) Port Kembla, Australia (500 kW)

Figure 1.1 Notable OWC examples from various locations around the world (Falcão, 2000; Heath et al., 2000; Alcorn et al., 2005)

On the other hand, oscillating body devices (OBs) present a diverse category of WECs that utilize wave-induced motion to drive mechanisms and generate power. The induced motion can be up-and-down, forward-and-backward, or other complex combinations, offering various design possibilities. This category includes point absorbers (buoys), terminators, and attenuators (line absorbers), each with unique features and potential. Notable examples of OBs can be found in Portugal, Hawaii, and Scotland, as shown in Figure 1.2, with rated capacities ranging from 315 kW to 2.25 MW (Cameron et al., 2010; Ocean Power Technologies, 2011; Energias de Portugal, 2021).

(a) Agucadoura, Portugal (2.25 MW)

(b) Oahu, Hawaii (1 MW)

(c) Orkney, Scotland (315 kW)

Figure 1.2 Notable OB examples from various locations around the world (Cameron et al., 2010; Ocean Power Technologies, 2011; Energias de Portugal, 2021)

Finally, overtopping devices (ODs), which operate similarly to hydropower plants, utilize the propagation of waves to direct water into elevated reservoirs and back to the ocean. Hydro turbines are utilized to generate power. Generally, these systems are less complex and can be deployed on- or off-shore (IRENA, 2020). An example of overtopping devices can be found in Denmark, as shown in Figure 1.3, with a maximum rated capacity of 10 MW (Christensen et al., 2005).

Figure 1.3 Notable OD example: The Wave Dragon, Denmark (Christensen et al., 2005)

Wave energy converters utilize power take-off (PTO) systems to convert wave energy into useful power by ultimately driving a generator. PTOs encompass various generator drive mechanisms, including mechanical, hydraulic, and pneumatic, as shown in the wave energy conversion scheme of Figure 1.4 (Ahamed et al., 2020).

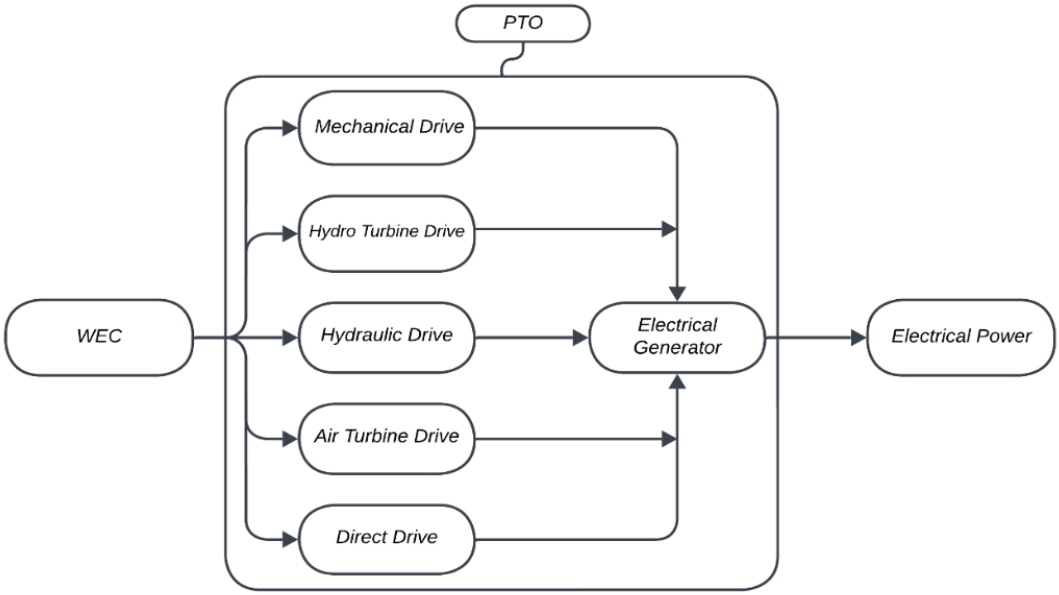

Figure 1.4 The general wave energy conversion scheme

Given the wide range of converter configurations shown in Figure 1.5, wave energy technologies have yet to converge on a standardized design. Consequently, depending on the configuration, reliable performance comparison data may be limited when evaluating a novel design. While numerous studies have been published on wave energy conversion, the practical application remains complex, particularly when analyzing diverse wave conditions. Currently, the primary focus of the existing literature is on developing and testing feasible WECs and assessing the availability of wave energy at various locations around the world (López et al., 2013).

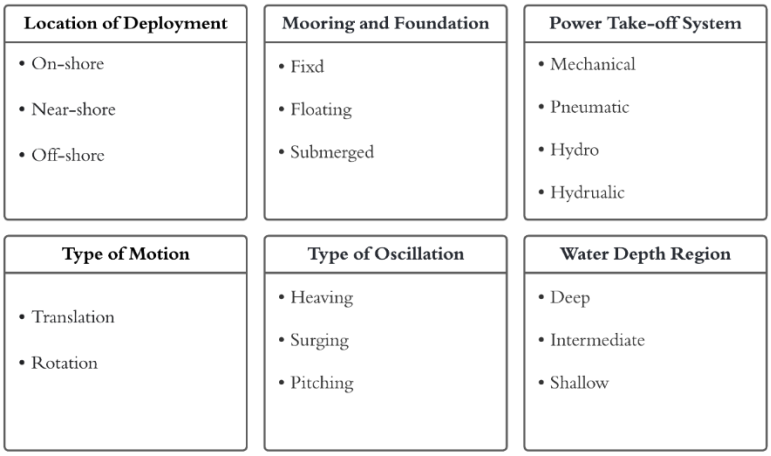

Figure 1.5 The various possible configurations of wave energy converters

Additionally, compared with other renewables, the upfront investment and infrastructure required to establish and maintain the aforementioned conventional converters are relatively substantial. Consequently, the search for more cost-effective alternatives continues to achieve large-scale commercialization. In this context, rotary wave energy converters are considered more straightforward and scalable, contributing to their growing popularity (Akimoto et al., 2014). Moreover, rotary converters differ from conventional converters in terms of their unidirectional rotational motion rather than oscillation, which may be either drag- or lift-induced depending on the geometry, as shown in Figure 1.6 (Jeans et al., 2013; Yang et al., 2018).

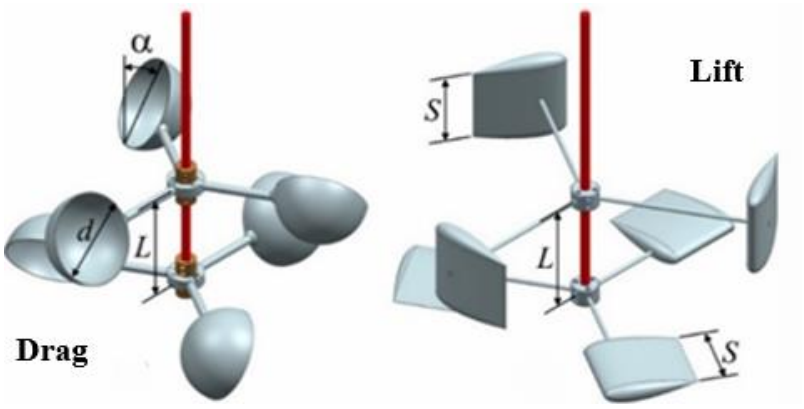

Figure 1.6 Sample drag and lift rotors for wave energy conversion (Yang et al., 2018)

Drag-type rotary wave energy converters are simple and inexpensive but tend to be less efficient. For example, semi-circular Savonius rotors moving in response to wave-induced differential drag fall into this category of WECs, providing a straightforward solution for harnessing wave energy. Conversely, lift-type converters are generally more efficient; however, they are more complex. Such systems typically employ cycloidal rotors that generate lift due to the circulation around a hydrofoil rotating within a wave-induced velocity field. Ultimately, the choice between the two depends on local wave conditions, intended application, and budget (Tutar & Veci, 2015; Yang, Diaz, et al., 2018; Yang et al., 2018; Ermakov & Ringwood, 2021).

1.2 Thesis Objectives

In this study, a novel rotary wave energy converter is proposed to address some of the limitations of both drag and lift converters. Initially developed by Selimoglu (2013), the design is registered under patent number WO2013180680. The proposed novel design is relatively simple and is thus expected to be more cost-effective than conventional converters for large-scale applications. Furthermore, the design utilizes drag and lift forces to combine the simplicity of drag-type converters with the higher efficiency of lift-type converters by incorporating a set of hinged blades that can self-adjust their orientation in response to incident waves.

The study investigates the power conversion performance of the converter at various conditions in an experimental wave flume to determine optimal characteristics and guide future design optimizations. The study further aims to provide a practical guide to the most common wave theories to shorten the gap towards achieving advancements in wave energy conversion. Per these aims, the thesis objectives are outlined below.

1. Experimentally investigate the proposed novel converter for proof of concept.
2. Identify optimal operational conditions and parametric combinations.
3. Develop a structured guide for theoretical wave calculations.
4. Analyze the experimental results with respect to wave theory.

2. LITERATURE REVIEW

The use of rotary devices for wave energy conversion initially emerged due to the orbital motion assumed by water particles within a wave train, as shown in the schematical wave representation of Figure 2.1. In principle, rotary converters can hydrodynamically capture this orbital motion to produce continuous rotation, eliminating the need for rectification stages used in oscillatory devices and enhancing power take-off efficiencies. As previously discussed, such converters are commonly categorized into drag-type and lift-type systems, each leveraging separate physical principles for energy extraction. Drag-based systems, such as Savonius rotors, utilize differential drag forces to generate torque. Meanwhile, lift-based systems, such as cycloidal rotors, rely on the lift force acting on a hydrofoil as it rotates through a velocity field (Faizal et al., 2010; Siegel et al., 2010; Ermakov & Ringwood, 2021).

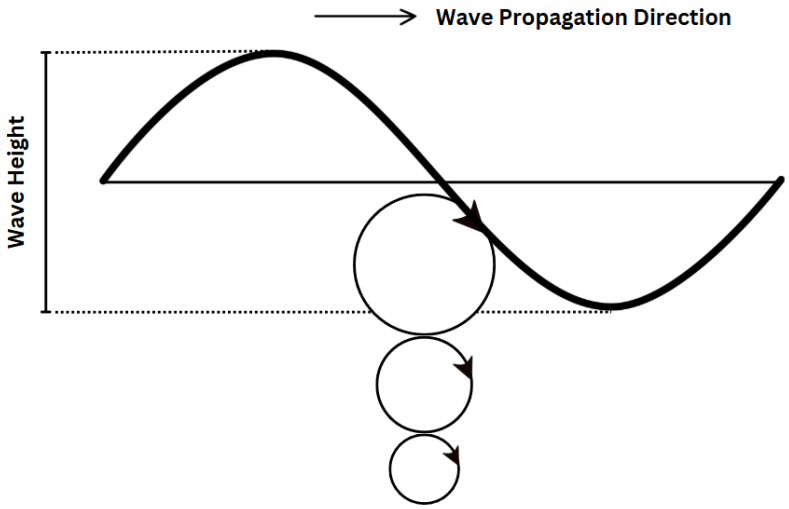

Figure 2.1 Schematical wave train showing the orbital motion of water particles

The following review explores several experimental and numerical studies on drag- and lift-based rotary wave energy converters, focusing on key findings, control techniques, and performance optimization strategies. It highlights current advancements and limitations and sets the stage for the present work.

2.1 Drag-Type Rotary Wave Energy Converters

The majority of studies on drag-type rotary wave energy converters are concerned with horizontal Savonius rotors, aiming to investigate the effects of operational parameters numerically and experimentally and to identify the optimal performance conditions in terms of conversion efficiency. A number of these studies are presented next.

In a study on a 300-mm long, five-blade Savonius converter, several wave conditions were tested at various rotor submergence levels in an experimental wave flume. Image velocimetry was used to observe the wave-rotor interactions, and the rotational speed was recorded. The rotational speed was found to increase with increasing wave frequency and height, that is, at low periods and increased heights. The maximum rotational speed was attained at a submergence level of 1.06D as particle orbits are larger near the surface. Wave heights increased with increasing frequencies up to 0.9 Hz, after which the waves started breaking. Finally, the velocity field was oriented downstream under the crest and upstream under the trough, creating orbital motion. The power output could not be measured directly due to the rotor's lightweight, which was unsuitable for practical load measurement techniques (Faizal et al., 2010).

Later, four similar rotors were tested in an array under similar conditions. The results showed that speed increased with frequency while increasing the spacing between the rotors decreased the rotational speed at low submergence levels. No pressure drops were observed in the domain; thus, no cavitation occurred on the blades (Ahmed et al., 2010). Seven similar rotors with blade angles ranging from 60 to 90 degrees were tested under similar conditions to optimize the preceding five-blade rotor design. The submergence level was varied, and the rotational speed was recorded. The results showed that the optimal blade curvature was 70°, at which the maximum rotational speed was obtained. Furthermore, arrays of rotors with the optimal angle were tested at different spacing and submergence levels. The optimal performance was obtained at a center-to-center spacing of 1.03D. The study concluded that the 90° rotor did not achieve full rotation and that the curved blades were more effective at capturing particle orbits as they were

more streamlined, allowing for maximum momentum transfer (Ahmed et al., 2013). The schematical representation of a Savonius converter is shown in Figure 2.2.

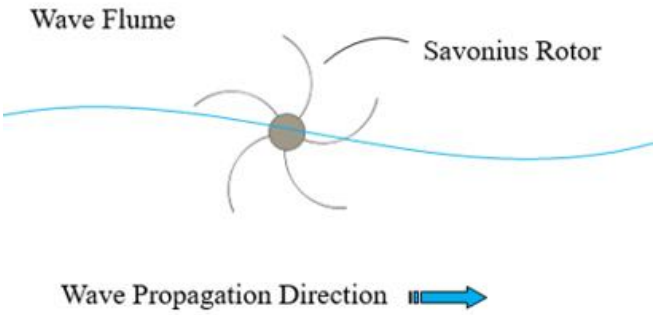

Figure 2.2 Schematical representation of a Savonius converter

In another study, Hindasageri et al. (2011) investigated varying the number of blades of a Savonius rotor, 150 mm in diameter, under shallow wave conditions at various submergence levels. It was shown that the three-blade rotor recorded a maximum rotational speed at zero submergence. In contrast, the five-blade rotor achieved maximum rotational speed at -5 cm submergence. At +5 cm submergence, the rotation became oscillatory due to flow discontinuities around the rotor. The rotational speed increased with wave height at zero submergence but was unaffected at the -5 cm level. Furthermore, at a wave height of 15 cm, equal to the rotor diameter, increasing the submergence level reduced the rotational speed of the three-blade rotor by 25% compared to its value at zero submergence; however, for the five-blade rotor, this doubled the rotational speed. The four-blade rotor had a negligible response.

Hindasageri et al. (2012) further investigated the five-blade rotor under a variety of operational conditions. The rotational speed was recorded, and the power was estimated using deadweights attached to a fixed pulley system. The rotational speed increased with increased wave heights and decreased wavelengths, while the efficiency increased with wave height but decreased with wavelength. Furthermore, a parametric analysis showed that the deadweight was the primary parameter affecting performance. The study suggested investigating arrays of multiple rotors and developing methods to increase differential drag, such as using a deflector plate or a breakwater structure,

which was investigated by Bikas et al. (2014), where tests were performed at various breakwater locations and rotor submergence levels. The deadweight mass was varied up to 600 g, and the resulting efficiencies were calculated. The maximum efficiency (6.8%) was achieved at a deadweight mass of 500 g at zero submergence. The optimal location for the breakwater structure was 10 m downstream of the rotor. Furthermore, it was observed that wave heights closer to the rotor's diameter resulted in higher efficiencies.

In a numerical study, Zullah and Lee (2013) investigated integrating a large-scale Savonius rotor into an OWC system using the CFD software Ansys CFX. The optimal rotational speed was estimated at 20 rpm using the Morrison equation and was kept constant in all simulations. The results showed that a blade curvature of 20º resulted in a maximum efficiency of 18.58%, demonstrating the potential for Savonius rotors to replace air turbines in OWCs.

Tutar and Erdem (2013) utilized a finite-volume model to investigate the performance of a three-blade Savonius rotor in a numerical wave flume (NWF) using the CFD software FLOW-3D. The D'Arcian model simulated porous media behavior in the damping domain, eliminating wave reflection. Second-order Stokes waves were generated with heights ranging from 100 mm to 160 mm at zero submergence. The results showed that wave height and frequency influenced the flow characteristics. At the same time, the rotational motion of the rotor was observed to be oscillatory, that is, clockwise and counterclockwise, due to flow discontinuities around the blades.

Later, Tutar and Veci (2015, 2016) performed experimental studies on Savonius rotors with a diameter of 252 mm under regular wave conditions in a 24 m-long experimental wave flume (EWF). Rotors with three, four, and five blades, shown in Figure 2.3, were tested at various submergence levels, and the rotational speed and torque were measured to calculate efficiency. The results indicated that increasing the wave height and number of blades while decreasing the wave period enhanced performance at zero submergence and below. In contrast, a positive submergence reduced performance due to wave overtopping. A wave height of 200 mm resulted in optimal performance at a wave

period of 3 s. Additionally, an array of the three-blade rotor was tested, and the optimal center-to-center spacing was found to be 450 mm.

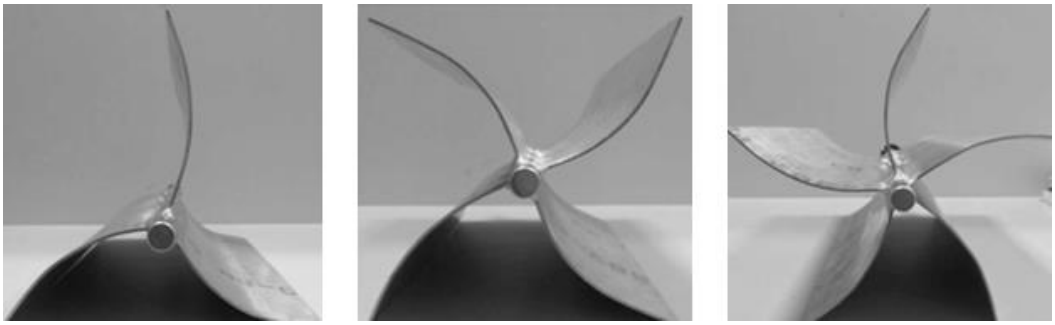

Figure 2.3 The rotors used by Tutar and Veci (2015) in their experimental study

Prasad et al. (2018) presented a numerical study on a three-blade Savonius converter 1.8 m in diameter and a length of 3 m under mean sea wave conditions (H = 2 m, T = 12.68 s) and three submergence levels (1.0D, 1.125D, and 1.25D) using Ansys CFX. The wave formations were validated against the Stokes theory and were in good agreement. The results showed that optimal performance was achieved at a submergence level of 1.0D, where the effect of the blade curvature was further investigated. A blade with a 20º curvature achieved maximum power output, which increased linearly to 37.5 rpm, peaking at 42.5 rpm before declining. The rotor produced lower power under minimum sea conditions but higher power up to 40 rpm under maximum sea conditions. The power output at maximum sea conditions (13.14 kW) was lower than at mean sea conditions (15.01 kW), indicating the critical role of the rotor-wave interaction in performance optimization. The maximum power was 15.01 kW at 42.5 rpm, with an efficiency of 16.7% under mean conditions. It is worth mentioning that sea conditions vary from one location to another, and the conditions used were of Ram et al. (2014).

Li et al. (2022) investigated a 400-mm long, two-blade Savonius rotor under various conditions, both numerically and experimentally. The optimal submergence level was determined to be 0.75D, at which the rotor was numerically modeled using three rotational control strategies: phase-locked strategy (PLS), initial phase-locked strategy (IPLS), and phase-unlocked strategy (PUS). In the PLS approach, the rotation of the rotor was synchronized with the frequency of the wave to maintain alignment between

the blade entry point and the wave crest. However, the PLS approach led to excessively high rotational speeds, reducing the torque transfer efficiency, and ultimately making the PLS approach the least effective strategy. In the IPLS approach, the rotor entered each wave cycle with a rotational frequency half of the wave. For a two-blade rotor, this aligned each blade with the wave crest or trough, achieving a balance that minimized energy loss and maximized power output. Finally, the PUS approach allowed the rotor to rotate freely without synchronization, which limited energy capture. Optimal performance was obtained under the IPLS approach with a maximum efficiency of 12.47% at a wave period of 1.3 s, maintaining a positive net torque. The study concluded that rotational control was critical for enhancing the conversion performance.

Subsequently, Li et al. (2023) presented an optimization study on the Savonius rotor under the IPLS approach to determine the effects of diameter, blade number, and blade thickness. Tests were performed in an experimental wave flume, followed by a numerical optimization model using STAR-CCM+ and assuming a transient, two-phase flow. The model was validated theoretically and experimentally. However, since the rotor was freely rotating in the experimental flume tests (PUS), the resulting torque signals were undetectable, but the rotational speed was recorded for comparison with the numerical results. The results showed that increasing wave height improved efficiency, while wave period variations adversely affected performance. Higher rotational speeds were observed for shorter wave periods, but conversion performance declined for wave periods below 1.2 s. The study suggested naming this phenomenon, attributed to nonuniform wave-induced flow fields, as the Relative Short Wavelength Impact (RSWI). It was noted that the RSWI could be mitigated when the wavelength-to-diameter (D/λ) ratio exceeded 17, stabilizing the wave-rotor interaction. Furthermore, the study defined optimal diameter-to-wave-height ratios across three stable wave steepness (H/λ) ranges, such that D/H = 2.25 for $0.082 \leq H/\lambda \leq 0.104$, D/H = 2.50 for $0.032 \leq H/\lambda \leq 0.067$, and D/H = 3.0 for $0.011 \leq H/\lambda \leq 0.018$. The ranges obtained resulted from a balance between the effects of the RSWI, which decreased with steepness, and the excessive tip speed observed for diameters exceeding these ranges. Additionally, increasing blade thickness generated higher torque at the blade edge but was outweighed by a reduction in torque from the blade side, reducing overall

efficiency. Rotors with more than two blades exhibited higher rotational speeds but generated lower torque, leading to a 60% reduction in efficiency in a four-blade rotor compared to a two-blade rotor. Finally, the optimal performance was achieved at a (D/H) ratio of 2.25 and a wave steepness (H/λ) of 0.104, yielding a maximum efficiency of 18.6%. The study emphasized that these findings are specific to rotors operating under the IPLS approach, which were demonstrated to enhance performance. The numerical domain used in the study is illustrated in Figure 2.4.

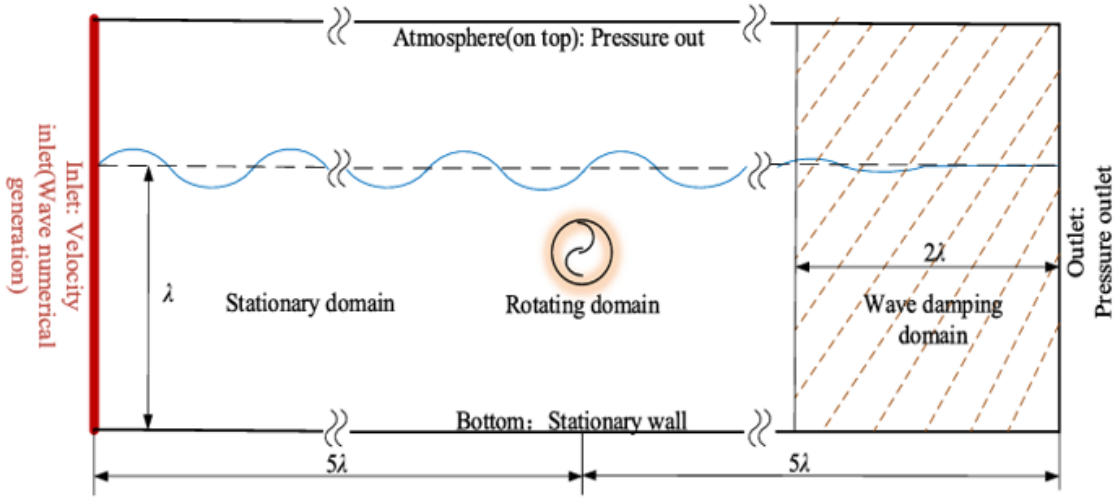

Figure 2.4 The numerical flow domain used by Li et al. (2023) in their study

2.2 Lift-Type Rotary Wave Energy Converters

Most studies on lift-type rotary wave energy converters are concerned with horizontal cyclorotors employing hydrofoils, aiming to optimize performance mathematically, numerically, and experimentally by investigating parameters such as pitch control, submergence, and rotational speed. Similarly, a number of these studies are presented.

In an experimental study, Pinkster and Hermans (2007) investigated the performance of a single-hydrofoil (NACA 0015) rotary converter in regular, long-crested wave conditions. The tests were conducted in a 200 m wave basin with a hydrofoil span of 1.5 m. The hydrofoil was mounted on a horizontal shaft and freely hinged between two end plates, facilitating stable rotational synchronization of the pitch angle with the incident

wave and eliminating the need for feedback control. As the waves passed the hydrofoil, the lift was generated perpendicular to the radial velocity vector, resulting in a rotational moment. The study revealed that the hydrofoil's rotation generated no upstream waves, while downstream wave heights were reduced, indicating wave termination. Finally, the shaft torque was found to depend on the circulation around the foil and had an almost constant signal. The system is shown in Figure 2.5.

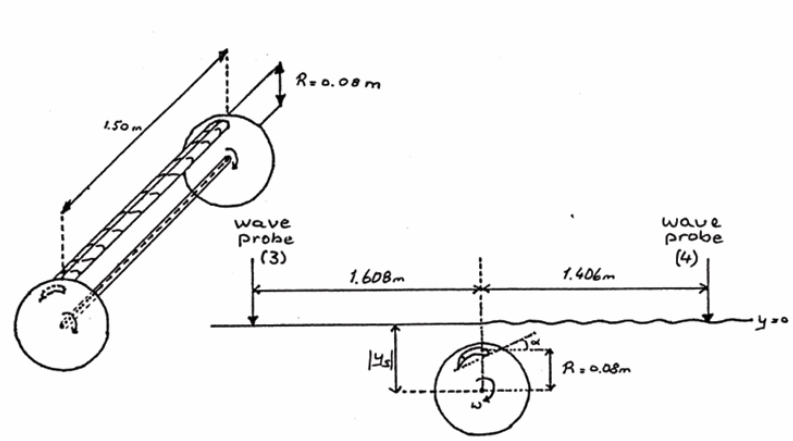

Figure 2.5 Schematical representation of the converter of Pinkster and Hermans (2007)

In a numerical study, Siegel et al. (2010) modeled a two-blade cycloidal wave energy converter under linear, intermediate-depth wave conditions using 2D potential flow simulations, treating the hydrofoils as point vortices. The study evaluated both the rotor's wave generation and wave terminator capabilities. A perfect wave terminator, as described, generates an incident wave in the opposite phase downstream, effectively canceling the wave. The results showed that optimal performance was achieved when the hydrofoil's tangential travel velocity matched the wave celerity, i.e., when the rotational speed matched the wave frequency. The optimal diameter was 0.318 times the wavelength, independent of water depth. The simulations did not consider losses from viscous skin friction and pressure drag, as they were estimated to account for less than 30% of the incident wave power. The study highlighted the potential for high-efficiency wave energy conversion and effective wave termination under idealized conditions, demonstrating an inviscid conversion efficacy of 95%.

Later, Siegel et al. (2012) experimentally investigated the cycloidal converter for irregular deep-water conditions in a small-scale flume. The rotational speed and pitch angle were synchronized with the incoming wave frequency and height, utilizing a feedback control scheme through wave gauges to optimize wave cancellation and lift generation. A sloped beach was used at the damping zone to minimize reflection, achieving a reflection coefficient, that is, a reflected-to-incident wave height ratio of approximately 0.11. The results showed that wave cancellation efficiencies of up to 80% with wave periods of 0.4 s to 0.75 s at a wave height of 20 mm were achieved. The wave profile data collected from the wave gages showed significant amplitude reduction between upstream and downstream measurements. The wave termination efficiency decreased when the ratio between the wave speed and the rotational speed diverged from unity. Direct shaft power measurements could not be performed due to the small scale used. The schematical representation of the experiment is shown in Figure 2.6.

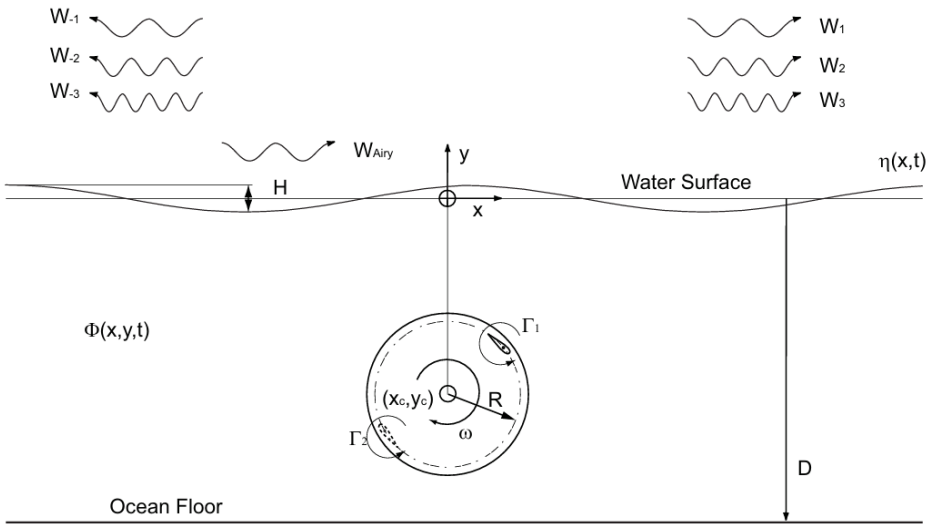

Figure 2.6 Schematical representation of the cycloidal converter of Siegel et al. (2012)

Finally, Siegel (2018) presented a numerical performance benchmarking study of the cycloidal converter. The study revealed that the cycloidal converter, CycWEC, outperformed many other converter designs, such as buoys, OWCs, and flap devices, especially regarding the device's energy conversion ratio per unit mass. Moreover, the full-scale cycloidal converter had the largest conversion span over other single WECs, extending 60 m in the wave crest direction. The device's continuous high-velocity ratio

enhanced its energy absorption since the required power take-off force decreases linearly with an increased velocity at the same power output. The suggested full-scale model had a diameter of 12 m and a chord length of 5 m, with an estimated 70% conversion efficiency at a mean annual absorbed power of 619 kW.

In a study by Folley and Lamont-Kane (2021), the behavior of hydrofoils was analyzed across different depths and wave conditions. The research demonstrated that, while 2D models achieved circular motion in deep water, finite-span hydrofoils followed elliptical trajectories due to variations in hydrodynamic damping. In contrast, shallower water conditions promoted more circular motion. The calculations showed that a 30-m-wide hydrofoil performed best at a submergence of 25 m and a wave period of 10 s. The study also pointed out the shortcomings of 2D hydrodynamic modeling and stressed the need for 3D analyses to achieve reliable designs.

In another study, Lamont-Kane et al. (2021) investigated the hydrodynamic performance of a lift-based two-blade converter, presenting a mathematical model to evaluate efficiency under regular wave conditions. The study found that up to 80% efficiencies were achievable, even with drag losses, surpassing many traditional designs. The efficiency increased with wave height up to a wave period of approximately 8 s, after which it declined with wave height. This behavior was attributed to the constraint imposed on the radius of rotation by the submergence level. The study noted that fixed-radius designs necessitated specific wave height and period combinations for optimal operation. Nonetheless, the system demonstrated substantial power output and stability under fixed-radius and pitch constraints, showcasing resilience to imperfect control. A sensitivity analysis showed that effective energy capture could be maintained across various wave conditions, provided the hydrofoils avoided opposing phase regimes when operating without proper pitch adjustments.

Ermakov et al. (2022a) mathematically investigated advanced control strategies for a two-hydrofoil cyclo-rotor converter to maximize energy capture. A two-dimensional mathematical model was used to optimize hydrofoil pitch angles and rotational speed in

both monochromatic and panchromatic wave conditions. The results showed that variable speed control alone enhanced energy capture by 30-40% in monochromatic waves. Conversely, combined pitch and speed control improved energy capture in panchromatic waves. The study highlighted the need for real-time control to optimize tangential forces and pitch angles, necessitating quick actuation but must be designed within the system's fatigue limits. Finally, wave prediction methods and more advanced servo systems were deemed essential for achieving such control schemes.

Ermakov et al. (2022b) noted that cyclorotors were traditionally operated at a constant speed with the wave frequency, and their performance has often been assessed through wave cancellation metrics. The study revealed that varying the rotational speed within the wave-passing period enhanced mechanical power generation, increasing shaft power by up to 46% in monochromatic waves but reducing wave cancellation effectiveness and increasing viscous losses. For the rotor geometry considered, the optimal angle of attack (15°) was kept constant, which resulted in the variable rotational speed converging to an alternating solution between half and double the wave frequency.

Olbert and Abdel-Maksoud (2023) developed a numerical model for lift wave energy converters to overcome the limitations of conventional potential flow and semi-analytical models. The model utilized the RANS approach integrated with the SST k-omega turbulence model modified to reduce artificial turbulence near the free surface and stagnation points and the γ-Reθ transition model to improve laminar-to-turbulent transitions and stall behavior. The validation included spatial and temporal discretization, wave propagation tests, and comparisons with experimental data, showing high accuracy in predicting surface forces at pitch angles. However, stall predictions were delayed due to boundary layer assumptions. Cyclorotor foils exhibited unique tangential forces, including positive forces even in calm wave conditions, caused by azimuthal load shifts and pitch moments, requiring precise modeling to predict shaft torque accurately. Wave radiation simulations showed that wave height decreased with deeper rotor submergence, while shallow submergences revealed challenges like rotor ventilation linked to numerical limitations. The study also found that simplified models assuming symmetrical lift and drag behavior were accurate only at small angles of

attack and failed under realistic conditions due to turbulence and flow separation. Comparisons with experimental data from the LiftWEC project confirmed the model's reliability in predicting hydrodynamic forces. However, the 2D simulations did not capture 3D effects, such as vortex dissipation, which influenced tangential forces.

After thoroughly reviewing the available literature on rotary wave energy converters, with a particular emphasis on drag-based systems such as horizontal Savonius rotors and lift-based systems such as cyclorotors, the following general statements can be made to summarize key findings and provide insights for the present work.

- Up to 18.6% conversion efficiency was achieved under optimal conditions for drag-based Savonius rotor systems, often requiring precise adjustments to blade curvature, rotor submergence, and wave parameters. Lift-based systems demonstrated up to 80% efficiencies in some instances, with pitch and rotational speed control playing a critical role in performance optimization.

- Increased wave heights and appropriate wave periods generally enhance energy capture, but high periods could reduce efficiency due to suboptimal interactions.

- Optimal submergence levels varied between rotor types, with drag-based systems performing best near or slightly below the mean water level. In contrast, lift-based systems benefited from moderate submergence to balance wave cancellation and tangential force optimization.

- Rotational speeds typically increased with wave frequency and height, but the fluctuating behavior necessitated advanced control schemes in both rotor types.

- Due to flow discontinuities, shallow submergences often introduce challenges, such as rotor ventilation (interaction with the air phase) or oscillatory rotation.

- Despite some limitations, numerical simulations provided valuable insights into rotor performance but were primarily presented in 2D instead of 3D.

3. METHODOLOGY

3.1 The Experimental Setup

3.1.1 System description and working principle

The novel rotary converter proposed in this study is an enhanced version of the original design developed by Selimoglu (2013). The converter is intended for near-shore operation and features a relatively simple structure that is potentially more cost-effective than conventional wave energy converters for large-scale applications. The rotor utilizes hinged hydrofoils that can self-adjust their orientation, as in Figure 3.1, to capture the wave-induced drag. In the present study, proof of concept is experimentally established, and torsional power capture is investigated relative to the theoretically available wave power under various conditions in a controlled experimental wave flume (EWF).

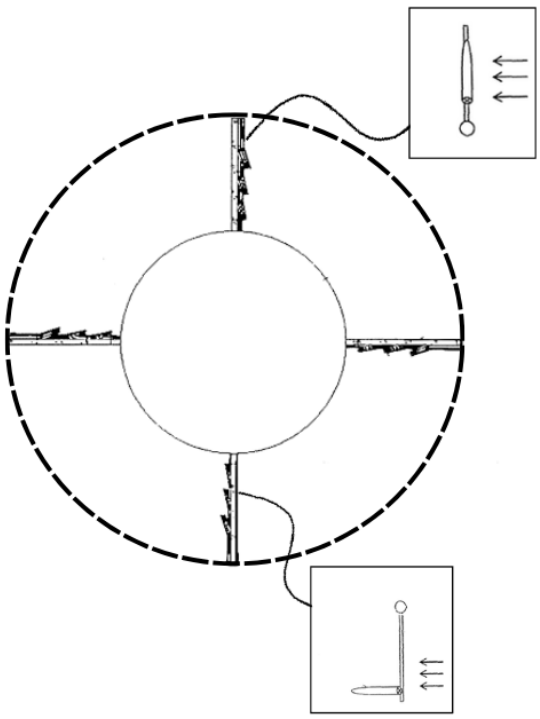

Figure 3.1 Schematical representation of the novel rotor (Selimoglu, 2013)

The rotor consists of 12 symmetrical 3D-printed hydrofoils hinged along their leading edge between two Ø300-mm circular plates using Ø4-mm steel shafts. Additionally, metal pins around the circular plates restrict the blades from rotating beyond the 90º mark. The rotor assembly measures 300 mm long and is mounted on a Ø20-mm steel shaft. The shaft is enclosed within a 1.8-mm-thick insulated PVC pipe to prevent corrosion while blocking the low-resistance central flow path, directing the flow toward the blades. The rotor's CAD model and assembly are shown in Figures 3.2 and 3.3.

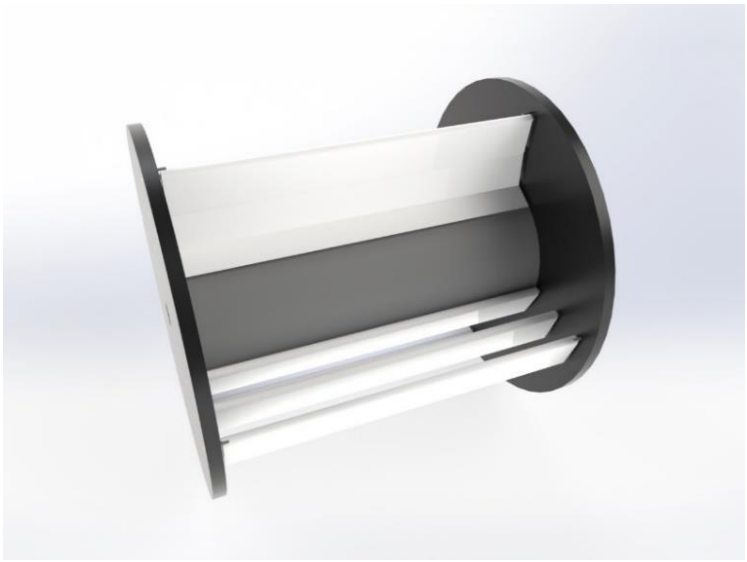

Figure 3.2 Rendered CAD model of the rotor assembly

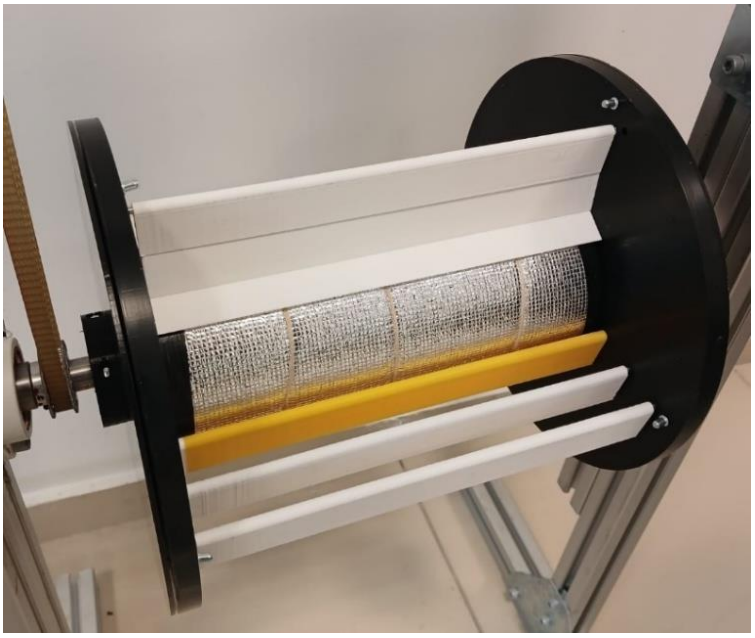

Figure 3.3 Finalized rotor assembly

The hydrofoils utilized in the rotor assembly are shown in Figures 3.4 and 3.5. As mentioned, each blade is freely hinged along its leading edge, enabling upward rotation up to the 90º mark, where metal stoppers restrict further rotation. Upon interaction with the incident wave, the flow is redirected around the rotor's midsection, causing the top blades to rotate upwards and lock at the 90º position, forming a barrier against which a drag force is applied. On the other hand, the returning bottom blades remain open, allowing the flow to pass freely between them, minimizing the generation of a reverse torsional moment. Furthermore, the returning blades experience a lift force that assists in reorientation to the upward position and ensures continuous operation.

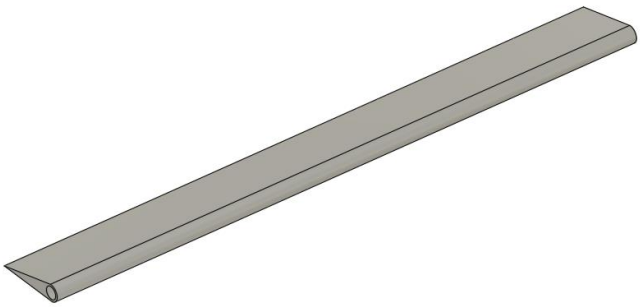

Figure 3.4 Isometric view of the hydrofoils used in the present rotor

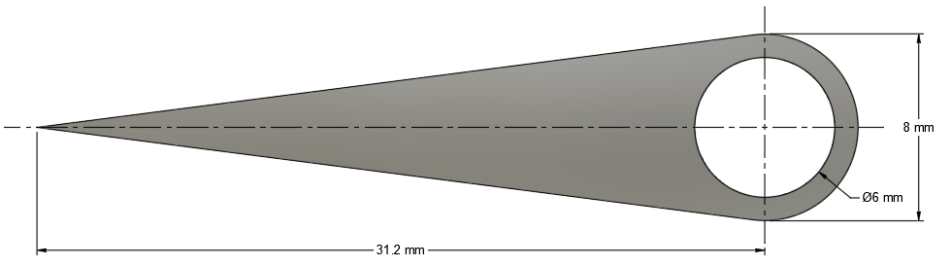

Figure 3.5 Geometry of the hydrofoil

The rotor assembly is supported by spherical flange bearings fixed between T-slot aluminum profiles, which make up the prototype's frame. A timing pulley system connects the rotor's shaft to a secondary upper shaft onto which an AC servo motor, a reduction gearbox, and a dynamic torque sensor are mounted. These components constitute the experimental prototype shown in Figures 3.6 and 3.7.

Figure 3.6 Rendered CAD model of the prototype assembly

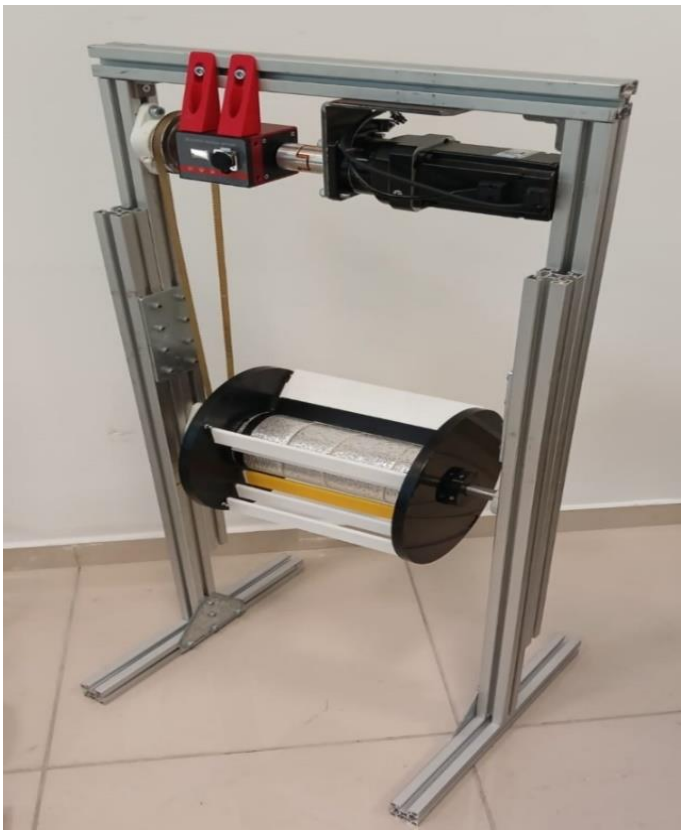

Figure 3.7 Finalized prototype assembly

The present prototype is intended for experimental torque measurement, necessitating a sufficiently large rotational moment of inertia to avoid rotational fluctuations and attain meaningful results (Tutar & Mendi, 2017). Typically, this would be achieved by upscaling the prototype using denser materials; however, it was constrained by the dimensions of the wave flume and available resources. Alternatively, an AC servo motor (750W Delta ECMA-C10807RS) facilitates unidirectional rotation, regulating the rotor's speed in proportion to the incident wave frequency and enabling dynamic torque measurements. The torque sensor (100 N.m Day Sensor DYN-200) utilizes an internal strain gauge that records the instantaneous torque difference while the motor maintains consistent rotational motion. The concept is analogous to using gearboxes and motorized braking mechanisms in wind turbines to balance torque and rotational speed. The motor speed is reduced by 1:10 through the reduction gearbox (Delta-PA090-C0108C1935), and a 1350-mm long timing belt is looped around a pair of timing pulleys (60:24-T5-16) to connect both shafts. The larger pulley is mounted on the upper shaft to amplify the wave-induced torque signal, and the overall rotational ratio is 4:1. The assembly drawing and major parts are illustrated in Figure 3.8.

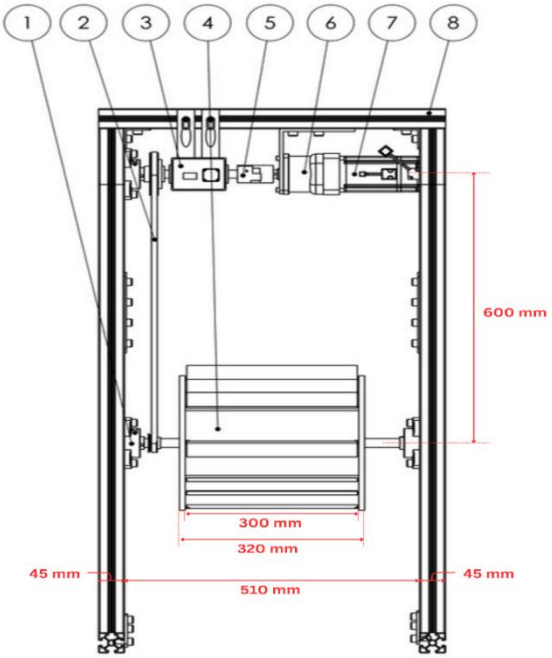

Figure 3.8 Assembly drawing: (1) Flange bearing; (2) Timing pulleys; (3) Torque sensor; (4) Rotor assembly; (5) Coupling; (6) Reductor; (7) Motor; (8) Aluminum frame

3.1.2 The experimental wave flume

Experiments were conducted in the Experimental Wave Flume (EWF) at the Ministry of Infrastructure and Transportation's Hydraulic Laboratory in Ankara, Türkiye. The 40-m-long flume measured 0.6 m in width, and 1.2 m in depth. It is constructed from sheet metal panels and steel profiles, with a glass section for observation near the end. The flume is equipped with a 7.5 kW servo piston-type wave maker capable of producing both regular and/or irregular waves. The stainless-steel plate has a stroke range of ± 0.5 m and can generate a significant wave height of up to 0.25 m at a wave period range of 0.7 to 2 s and a mean water level of 1.0 m. Furthermore, wave height and surface elevation are measured at various points using capacitance-type wave height meters (KENEK CHT7-50E / CH-406A) operating at a 50-millisecond sampling rate. The measurements are used to validate the generated waves against theoretical wave profiles. Finally, a sloped wave-absorbing structure is placed at the end of the flume to minimize reflections. The flume is illustrated in Figures 3.9 through 3.12.

Figure 3.9 The experimental wave flume at the AYGM hydraulic laboratory

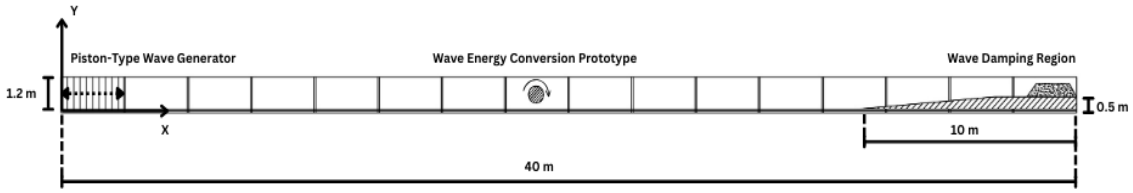

Figure 3.10 Schematical representation of the experimental wave flume

Figure 3.11 The interior of the wave flume showing the wave gauges

Figure 3.12 The wave damping region of the present experimental wave flume

3.1.3 Experimental conditions and data acquisition

In the present study, regular, steadily propagating design waves were generated at various parametric combinations to investigate optimal performance. The wave height (H) and wave period (T) values were adjusted from 10 cm to 20 cm and from 2 s to 5 s, respectively, according to the operational limits of the wave flume. The water depth (d) was set as 60 cm for all cases, and four submergence levels were considered. The submergence was adjusted by vertically shifting the assembly through the aluminum

frame to align the rotor's shaft relative to the free surface. The specifications and conditions are summarized in Table 3.1. Furthermore, the prototype was positioned at the center of the flume parallel to the wavefront, as shown in Figure 3.13. This placement allowed sufficient distance for the wave train to fully develop before reaching the system, as observed using the upstream wave gauge.

Table 3.1 Wave flume specifications and operational conditions used in the present study

Total Flume Length [m]	40
Internal Flume Width [m]	0.6
Flume Wall Height [m]	1.2
Water Depth [cm]	60
Wave Height Range [cm]	10, 20
Wave Period Range [s]	2, 3, 4, 5
Rotor Submergence Level [cm]	0, -10, -15, -20

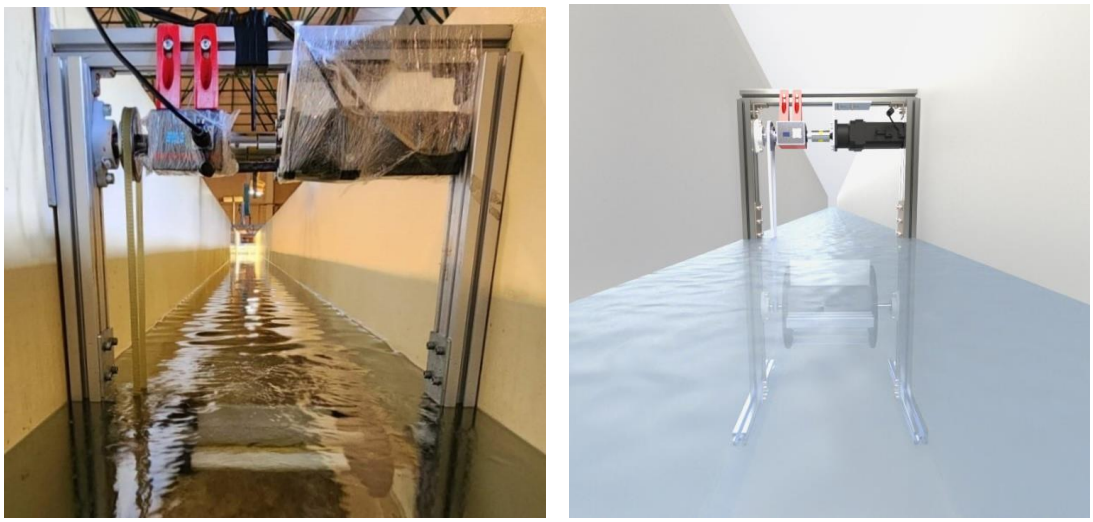

Figure 3.13 The test section of the EWF and its rendered CAD model

Additionally, the servo motor controlled the rotational speed to maintain unidirectional rotation and facilitate dynamic torque measurement. The motor speed is reduced by a factor of 10 through the reduction gearbox and amplified by a factor of 2.5 through the timing pulleys, and thus, the rotor turns at a quarter of the speed. The rotor speed was

adjusted in proportion to the angular frequency of the wave and was set to 0.5, 0.7, and 0.9 of its value for each experimental run. The set values, summarized in Table 3.2, were calculated according to Equations 3.1 and 3.2 (Fenton, 1990) and input to the motor through the control unit using the software ASDA SOFT V5.5.

$$N_{motor} = 4\, N_{rotor} \tag{1}$$

$$N_{motor} = 4\, \omega \left(\frac{60}{2\pi}\right) Ratio = 4 \left(\frac{2\pi}{T}\right)\left(\frac{60}{2\pi}\right) Ratio = \frac{240\ Ratio}{T} \tag{2}$$

Where N_{motor} and N_{rotor} are the motor's and rotor's rotational speeds in [RPM], ω is the angular wave frequency in [rad/s], T is the wave period in [s], and the ratio is either 0.5, 0.7, or 0.9 of the incident wave frequency.

Table 3.2 The rotational speed set values used in the experimental study

Wave Period [s]	Angular Frequency [rad/s]	Ratio	N_{Motor} [RPM]	N_{Rotor} [RPM]
2	3.14	0.5	60	15
		0.7	84	21
		0.9	108	27
3	2.09	0.5	40	10
		0.7	56	14
		0.9	72	18
4	1.57	0.5	30	7.5
		0.7	42	10.50
		0.9	54	13.50
5	1.26	0.5	24	6
		0.7	33.60	8.40
		0.9	43.20	10.80

Instantaneous torque and rotational speed were recorded during all experiments using the dynamic torque sensor and servo motor software. The torque sensor utilizes an internal strain gauge to measure the instantaneous net torque between the wave- and motor-induced torsional moments. The direction of the net torque was indicated by its sign, with a net positive value indicating a wave-induced net torque. Internal torque fluctuations caused by rotational friction or backlash were measured under wave-free conditions and set as the base level before all experiments. Additionally, ten wave cycles were allowed to pass before recording data to ensure that each wave train was fully

developed. The average net torque and average power were calculated from the recorded signals, and the efficiency was calculated relative to wave theory, according to Equations 3.3 and 3.4. The details of the theoretical calculations are discussed next.

$$P_{avg} = \left(\frac{2\pi}{60}\right) \tau_{avg-net}\, N_{sensor} = \left(\frac{2\pi}{60}\right) \tau_{avg-net}\, (0.1\, N_{motor}) \tag{3}$$

$$\eta = \frac{P_{avg}}{P_{th}} \tag{4}$$

3.2 The Theoretical Model

3.2.1 A brief introduction to wave theory

The water waves under consideration in this study are surface gravity waves, which appear between fluid layers having different densities: air and water. They result from wind blows that initiate the waves, while gravity acts to restore the mean level. The description of the propagation of these waves involves nonlinear effects, which must be simplified for simplicity. Compressibility, shear currents, and uneven ocean floors add to this complexity. In that regard, the description adopted in this study assumes that the floor over which the waves propagate is flat and impermeable and that the flow is two-dimensional, inviscid, irrotational, and incompressible. Thus, an approximate solution corresponding to a single, steady wave train propagating without change of form is achievable. This is the steady wave problem (Lighthill, 1978; Sobey et al., 1987).

Based on the wave parameters, a suitable steady wave theory is selected from the literature according to the depth region and wave-breaking limits. Surface gravity waves are classified into three depth regions, with the widely accepted criteria outlined below, where d and λ represent the water depth and wavelength, respectively.

$$Characteristic\ Depth\ Region \begin{cases} d/\lambda \geq 0.5 & Deep\ Water\ Wave \\ 0.05 < d/\lambda < 0.5 & Intermediate\ Water\ Wave \\ d/\lambda \leq 0.05 & Shallow\ Water\ Wave \end{cases}$$

The applicability ranges of the different theories are shown in Figure 3.14. The figure indicates a spectrum and serves as a graphical theory selection tool. However, the approach becomes tedious when multiple wave conditions are to be considered, and a more reliable quantitative selection method is needed. Nonetheless, two theories cover the entire spectrum: the Stokes and Cnoidal theories. These theories are nonlinear and can be formulated in any higher order, but the fifth order offers acceptable accuracies over most wave ranges, and higher orders are rarely used (Fenton, 1990).

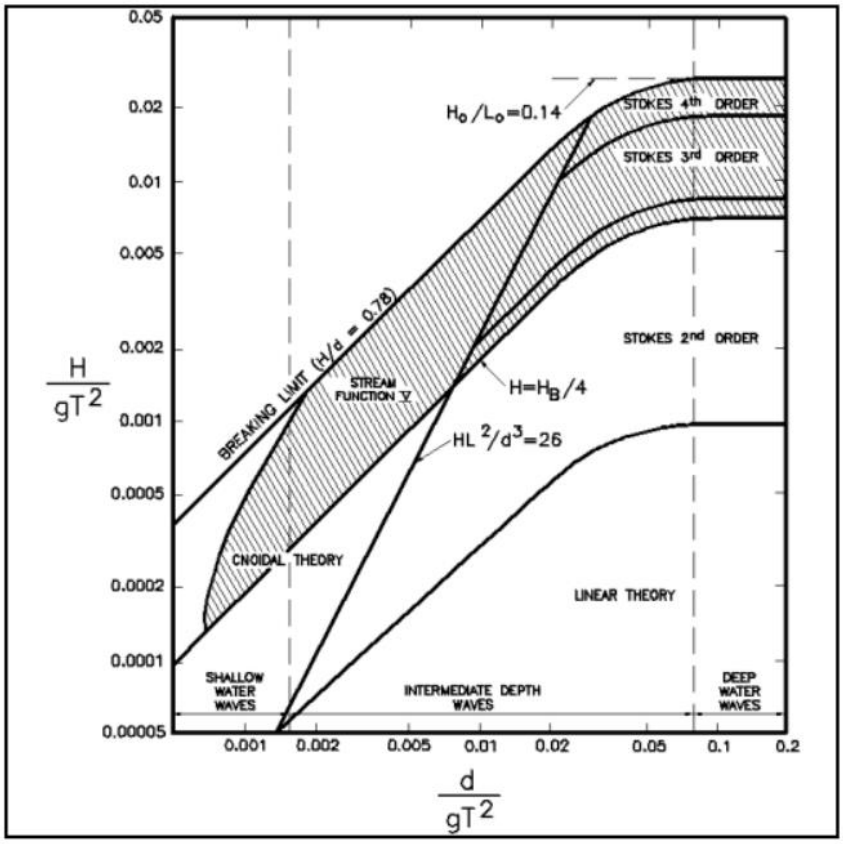

Figure 3.14 The applicability ranges of various wave theories (Méhauté, 1976)

To apply any wave theory, several parameters need to be known a priori. These include water depth, wave height, wavelength, and wave period. Furthermore, it is also necessary to have information on the wave speed, current, or mass flux since, depending on the reference frame, the wave speed varies to a stationary observer and is influenced by either current or mass flux. In that regard, the wave propagation problem can be formulated in a frame moving with the waves so that the wave celerity need not be defined in that frame. However, since the problem is viewed from a stationary frame, an assumption about the wave speed must be made to relate the two frames; otherwise, the wave speed should be measured (Rienecker & Fenton, 1981).

In the present study, the waves were generated within a closed wave flume. Consequently, the overall water mass flux was zero, and the related theories were formulated based on Stokes' second approximation of wave speed, as discussed later in this chapter. Known parameters included the mean water level of 0.60 m, wave periods, and wave heights. The wavelength, wave celerity, and current were unknown. The formulations adopted in this study were those of J. D. Fenton, but the mathematics involved in deriving the formulations were beyond scope (Fenton, 1990). Nevertheless, this discussion provides a framework for applying higher-order nonlinear steady wave theories to calculate the wave's mean energy flux and surface elevation.

3.2.2 Initial wavelength calculations

Since the wavelength was unknown, an initial calculation was required to determine the depth region and select a suitable wave theory for each wave condition under consideration. Fenton and McKee (1990) reviewed several wavelength approximations. However, all of these were based on linear dispersion, neglecting mean current effects. Their review proposed a new algorithm incorporating these effects, achieving acceptable engineering accuracy. The dispersion relation, upon which wavelength approximations were based, describes the relationship between wavelength and period. In actual sea conditions, wave trains consist of multiple wavelengths traveling at different speeds. Wave speed is sometimes referred to as phase velocity or celerity,

while the collective speed at which a group of waves travels is known as group velocity. The wave energy propagates at this group velocity. When waves with different periods travel at varying speeds, the wave train becomes dispersive, causing wave energy to spread spatially and temporally. Conversely, the wave train is considered non-dispersive if the group velocity is approximately independent of wave periods, as in shallow water waves (Han, 2015). According to Fenton and McKee (1990), the linearized dispersion relation, including current, can be written as follows:

$$\left(\frac{k}{g}\right)^{1/2} \bar{u} - \frac{2\pi}{T(gk)^{1/2}} + C_0 = 0 \tag{5}$$

Where $\bar{u}$ is the mean current, k is the wave number or dimensionless wavelength ($2\pi/\lambda$), T is the wave period, d is the water depth, g is the gravitational acceleration, and C_0 is a function of kd and is equal to $\sqrt{tanh(kd)}$. Substituting and using the angular wave frequency notation $\omega = 2\pi/T$, Equation (5) can be rewritten as follows:

$$\bar{u}k - \omega + \sqrt{gk \tanh kd} = 0 \tag{6}$$

In the limits where $\bar{u} \to 0$, that is, when the effects of mean current are neglected, Equation (6) reduces to the dispersion relation of the linear (Airy) wave theory and can be further simplified as follows:

$$\omega - \sqrt{gk \tanh kd} = 0 \tag{7}$$

Rewriting Equation (7) in terms of wavelength, the well-known wavelength formulation of the linear theory is obtained as:

$$\lambda = \begin{cases} \dfrac{gT^2}{2\pi} & Deep & tanh\,(kd) \approx Unity \\ \dfrac{gT^2}{2\pi}\, tanh\left(\dfrac{2\pi d}{\lambda}\right) & Intermediate & Solve\ Iteratively \\ \sqrt{gd}\, T & Shallow & tanh\ (kd) \approx kd \end{cases} \tag{8}$$

Equation (8) was the focus of the approximations reviewed by Fenton and McKee (1990). The relation can be applied by calculating the deep-water wavelength value and using it as an initial guess in the intermediate wavelength relation. The calculation is then iterated until a deviation of less than 0.0001 is achieved.

Among the linear dispersion relation approximations reviewed by Fenton and McKee (1990), Hunt's approximation was one of the most accurate across all wavelengths. The formulation presented by Hunt (1979) was found to be exact for deep and shallow waves and is given as:

$$(kd)^2 = \left(\frac{\omega^2 d}{g}\right)^2 + \frac{\left(\frac{\omega^2 d}{g}\right)}{1 + \sum_{n=1}^{\infty} d_n \left(\frac{\omega^2 d}{g}\right)^n} \tag{9}$$

Where the coefficients (d_n) from n = 1 to 6 are as follows (truncated after the 6th value):

$$d_1 = 0.6666666667 \quad d_2 = 0.3555555556 \quad d_3 = 0.1608465608$$

$$d_4 = 0.0632098765 \quad d_5 = 0.0217540484 \quad d_6 = 0.0065407983$$

Additionally, Fenton and McKee (1990) proposed another approximation for the linear dispersion relation to determine the wave number (wavelength). This approximation was exact for short and long waves, with a maximum error of 1.70% in the intermediate-depth range. It is expressed as:

$$k = \frac{\omega^2}{g}\left(\coth\left(\omega\sqrt{d/g}\right)^{3/2}\right)^{2/3} \tag{10}$$

Among the approximations reviewed by Fenton and McKee (1990), none accounted for the effects of mean current, which may be present in wave propagation. When information about the mean current is unavailable, it can be assumed to be small enough to be set to zero, with the assumption later justified through direct calculations from wave theory. However, obtaining measurement data is more accurate and relatively straightforward, as the current can be measured using a stationary velocity meter.

To account for the current term, Fenton and McKee (1990) proposed an enhanced approximation algorithm based on the linearized dispersion relation. The formulation of the algorithm is as follows:

If $T\sqrt{g/d} < 4$, then the initial wave number should be calculated from:

$$k_0 = \frac{4\omega^2/g}{\left(1+\sqrt{1+4\bar{u}\omega/g}\right)^2} \tag{11}$$

Otherwise, it should be calculated from:

$$k_0 = (1/d)\left[\frac{\omega\sqrt{d/g}}{1+F} + \frac{\left(\omega\sqrt{d/g}\right)^3}{6(1+F_{Froude})^4} + \frac{(11-19F)\left(\omega\sqrt{d/g}\right)^5}{360(1+F_{Froude})^7}\right] \tag{12}$$

Where F_{Froude} is the Froude number ($\bar{u}/\sqrt{gd}$). The wave number is then iteratively calculated from the below equation:

$$k_{n+1} = \left(\frac{1}{d}\right)\left[\frac{2\left(\sqrt{k_n d\ tanh\ k_n d}\right)\left(\omega\sqrt{d/g}\right) - (k_n d\ tanh\ k_n d) + (k_n d)^2 - (k_n d\ tanh\ k_n d)^2}{2\left(\sqrt{k_n d\ tanh\ k_n d}\right)\left(\bar{u}/\sqrt{gd}\right) + (tanh\ k_n d) + k_n d(1-(tanh\ k_n d)^2)}\right] \tag{13}$$

Fenton and McKee (1990) noted that the algorithm converged in fewer than two iterations. While other approximations exist in the literature, those presented in the foregoing section are deemed adequate in terms of their engineering accuracy, with minimal variations encountered between them. In the present study, Equation (13) is utilized to approximate the wavelength, assuming a zero current ($\bar{u} = 0$).

3.2.3 Wave theory selection criteria

After approximating the wavelength using the linear dispersion relation, a suitable wave theory is selected relative to specific wave parameters. As discussed, the Stokes and Cnoidal wave theories encompass the entire wave spectrum within their respective

applicability limits. The criteria outlined next provide a systematic approach for determining which theory of the two is applied to each wave condition.

The first criterion is based on Fenton's limiting wavelength (Fenton, 1990), defined as:

$$\lambda_{limiting} = 21.5\, d\, e^{-1.87\, H/d} \tag{14}$$

Where H is the wave height, and d is the mean water depth. The Cnoidal wave theory is applied if the approximate wavelength calculated from the dispersion relation exceeds the limiting value given by Equation (14). Conversely, the Stokes wave theory is used if the wavelength is smaller than this limiting value (Fenton, 1990).

In addition, Fenton (1990) proposed an empirical formula to calculate the theoretical maximum unbroken wave height for a given length and depth:

$$H_{max} = (d)\left(\frac{0.141063\left(\frac{\lambda}{d}\right) + 0.0095721\left(\frac{\lambda}{d}\right)^2 + 0.0077829\left(\frac{\lambda}{d}\right)^3}{1 + 0.0788340\left(\frac{\lambda}{d}\right) + 0.0317567\left(\frac{\lambda}{d}\right)^2 + 0.0093407\left(\frac{\lambda}{d}\right)^3}\right) \tag{15}$$

Experimental results reported in the literature indicate that the maximum attainable wave height upon breaking is approximately 0.55d. These findings suggest that, under experimental conditions, waves seldom reach the theoretical maximum described by Equation (15), likely due to physical constraints and instabilities inherent to the experimental setups (Méhauté et al., 1968; Nelson, 1987; Fenton, 1990).

The second criterion uses Hedges' limiting Ursel number (Hedges, 1995), defined as:

$$U_{Ursel} = \frac{H\lambda^2}{d^3} = 40 \tag{16}$$

Where H is the wave height, λ is the wavelength, and d is the mean water depth. The Ursel number represents the ratio of wave nonlinearity to shallowness and is defined as:

$$U_{Ursel} = \frac{Nonlinearity}{Shallowness} = \frac{H/d}{(d/\lambda)^2} \tag{17}$$

Using Equation (17), the Ursel number is calculated based on the approximate wavelength obtained from the dispersion relation. If it is less than 40, the Stokes wave theory is appropriate. Otherwise, the Cnoidal wave theory should be applied.

The third criterion is Goda's universal wave number (Goda, 1983), defined as:

$$U_p = \left(\frac{H}{\lambda}\right)(\coth kd)^3 \tag{18}$$

The wavelength and wave number used in Equation (18) are calculated using linear theory. If the resulting value is approximately 0.2 or less, the 3rd-order Stokes wave theory is deemed appropriate. Otherwise, the 2nd-order Cnoidal theory is applied. Nonetheless, to ensure consistency and accuracy, the present study follows the 5th-order formulation of Fenton (1990) for both the Stokes and Cnoidal theories. Finally, it should be noted that this experimental criterion might conflict with the previous two for specific wave conditions, and caution is advised when applying it.

3.2.4 Frames of reference and governing equations

A wave train consisting of a single, regular wave can be fully specified if the mean water depth, the wave height, the wavelength, and the wave period are known. Furthermore, measurements or approximations for the mean current are required since, for an inertial observer, the wave period shifts depending on wave speed, which depends on the mean current. This is known as the Doppler effect, the apparent change of wave period due to motion relative to a stationary observer (Fenton, 1990). Consequently, specific definitions must be made when formulating the theories to relate the velocity terms in various reference frames. Consider the wave train shown in Figure 3.15, where the inertial reference frame is denoted as (x, y), and the waves propagate at a velocity relative to this frame. Conversely, the non-inertial frame of reference (X, Y) moves with the waves at the same velocity. The theories are formulated in the non-

inertial frame and subsequently related to the inertial frame from which the waves are observed. The coordinates and velocity components of the two frames are as follows:

$$x = X + ct \quad and \quad y = Y \tag{19, 20}$$
$$u = U + c \quad and \quad v = V \tag{21, 22}$$

Where c is the wave speed, t is the elapsed time, u is the horizontal velocity component in the inertial frame (measured by a stationary observer), U is the horizontal velocity component in the non-inertial frame, v is the vertical velocity component in the inertial frame, and V is the vertical velocity component in the non-stationary frame of reference.

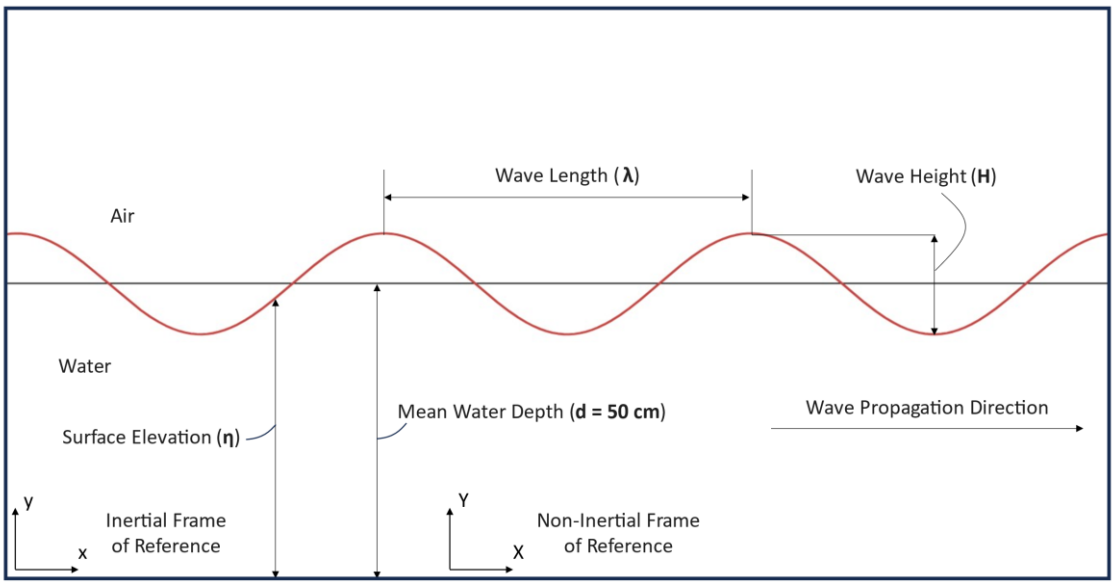

Figure 3.15 The wave train considered showing the reference frames and wave parameters

From a frame moving along the wave at the same velocity, the apparent steady flow beneath the stationary surface profile is directed in opposite to wave propagation, and the mean horizontal velocity is denoted by $-\bar{U}$. In contrast, in an inertial frame of reference, the mean horizontal velocity, denoted by $\bar{u}_1$, corresponds to the mean current measurable with a stationary sensor. The following equation relates the two frames of reference (Fenton, 1990).

$$\bar{u}_1 = c - \bar{U} \tag{23}$$

Subscript 1 refers to Stokes' first approximation of wave speed, which assumes that the average flow speed beneath the wave trough is zero, indicating no current ($\bar{u}_1 = 0$). If the mean current is zero, then $c = \bar{U}$ (Stokes' 1st approximation).

Alternatively, the two frames of reference can be related using the depth-integrated mean fluid velocity, $-Q/d$, where Q represents the volumetric flow rate per unit width [(m^3/s)/m]. From an inertial frame, the mean horizontal velocity also referred to as the mass-transport velocity $\bar{u}_2$, is expressed as:

$$\bar{u}_2 = c - Q/d \tag{24}$$

The subscript 2 corresponds to Stokes' 2nd approximation for wave speed. Under zero mass transport (e.g., in a closed wave flume), $\bar{u}_2 = 0$, and the wave speed is simplified to $c = -Q/d$, as in the present study (Fenton, 1990).

From a dynamic reference frame and under assumptions of inviscid, irrotational, and incompressible flow, a stream function ψ exists, with velocity components $U = \partial\psi/\partial Y$ and $V = -\partial\psi/\partial X$ satisfying the Laplace equation for potential flow, given as:

$$\frac{\partial^2\psi}{\partial X^2} + \frac{\partial^2\psi}{\partial Y^2} = 0 \tag{25}$$

Since no flow passes through the flume's bed at $y = 0$, and the free surface at $y = \eta(X)$ is itself a streamline with constant pressure, the boundary conditions for obtaining a solution of Equation (25) are written as:

$$\psi(X, 0) = 0 \tag{26}$$

$$\psi\big(X, \eta(X)\big) = -Q \tag{27}$$

$$\frac{1}{2}\left[\left(\frac{\partial\psi}{\partial X}\right)^2 + \left(\frac{\partial\psi}{\partial Y}\right)^2\right]_{Y=\eta(X)} + g\eta(X) = R \tag{28}$$

Where R is a constant, and Equations (25) through (28) constitute the governing equations to the steady wave problem. The derivation of the solution to these equations is out of the present scope, and the finalized formulations are presented directly.

3.2.5 Linear wave theory

The linear (Airy) theory describes the propagation of low-amplitude surface gravity waves based on inviscid, incompressible, and irrotational flow assumptions, allowing for a simplified mathematical treatment of wave motion. Although the focus of the present model is the fifth-order formulation of nonlinear wave theory, the key equations of linear theory are provided below to offer context for the Stokes and Cnoidal theories and to benefit the interested reader (Dean & Dalrymple, 1991).

As previously discussed in Equation (8), the wavelength is iteratively calculated from the linear dispersion relation, which can be rewritten as:

$$\lambda = \frac{gT^2}{2\pi}\ tanh(kd) = \frac{gT^2}{2\pi}\ tanh\left(\frac{2\pi d}{\lambda}\right) \tag{29}$$

From an inertial frame of reference, the surface elevation, representing the instantaneous displacement of the free surface, can be expressed as:

$$\eta\ (x,t) = \frac{H}{2} cos(kx - \omega t) = \frac{H}{2} cos\big(k(x - ct)\big) \tag{30}$$

In linear theory, kinetic and potential energies are equal and the mean energy density over one wavelength in [J/m^2] can be expressed as follows:

$$E = E_P + E_K = \frac{\rho g H^2}{16} + \frac{\rho g H^2}{16} = \frac{\rho g H^2}{8} \tag{31}$$

Finally, the mean energy flux per unit crest width in [W/m] is expressed as follows:

$$F = Ec_g = \frac{\rho g H^2}{8}\left[\frac{1}{2}c\left(1 + \frac{2\,kd}{sinh(2\,kd)}\right)\right] = \frac{\rho g H^2 \lambda}{16T}\left(1 + \frac{2\,kd}{sinh(2\,kd)}\right) \quad (32)$$

Where c_g is the group velocity. To automate the calculation, the linear formulation was compiled into a MATLAB code given in Appendix 1.

3.2.6 Stokes wave theory

The Stokes wave theory is a nonlinear, higher-order theory initially proposed by Stokes (1847). It integrates additional higher-order corrective terms (harmonics) into the solution of the linear theory to enhance its accuracy. While the theory can be expanded to any hypothetical order, the 5th-order formulation is generally sufficient for engineering purposes. However, the theory performs poorly in shallow water and is primarily intended for deep-to-intermediate depth applications (Holthuijsen, 2007).

The formulation is based on a perturbation expansion of a Fourier series in terms of wave steepness (ε = kH/2). From a non-inertial frame, the mean horizontal velocity is given as (Fenton, 1985):

$$\bar{U}(k/g)^{1/2} = C_0 + \varepsilon^2 C_2 + \varepsilon^4 C_4 \quad (33)$$

Substituting Equation (33) into (23), with $c = \lambda/T$, $\lambda = 2\pi/k$, and rewriting the equation, the higher-order dispersion relation is written as:

$$\left(\frac{k}{g}\right)^{1/2} \bar{u}_1 - \frac{2\pi}{T(gk)^{1/2}} + C_0 + \left(\frac{kH}{2}\right)^2 C_2 + \left(\frac{kH}{2}\right)^4 C_4 = 0 \quad (34)$$

Where the terms C_0, C_2, and C_4 are functions of kd, and are given in Appendix 2.

Similarly, if the formulation is based on the depth-integrated mean velocity, the higher-order volumetric flow rate per unit width can be expressed as:

$$Q\left(\frac{k^3}{g}\right)^{1/2} = C_0 \cdot kd + \left(\frac{kH}{2}\right)^2 (C_2 \cdot kd + D_2) + \left(\frac{kH}{2}\right)^4 (C_4 \cdot kd + D_4) \qquad (35)$$

Substituting Equation (35) into (24), with $c = \lambda/T$, $\lambda = 2\pi/k$, and rewriting the equation, gives:

$$\left(\frac{k}{g}\right)^{1/2} \bar{u}_2 - \frac{2\pi}{T(gk)^{1/2}} + C_0 + \left(\frac{kH}{2}\right)^2 \left(C_2 + \frac{D_2}{kd}\right) + \left(\frac{kH}{2}\right)^4 \left(C_4 + \frac{D_4}{kd}\right) = 0 \qquad (36)$$

Again, the terms C_0, C_2, C_4, D_2, and D_4 are functions of kd, given in Appendix 2.

Equations (35) and (36) can be solved for the wave number by applying a suitable numerical method such as the secant or bisection methods. The linear, deep-water wavelength result of Equation (8) and the approximate wave number result of the linear dispersion relation, previously obtained from Equation (13), can be used as initial or bracketing values for the numerical solution.

The solution adopted in this study flows from Equation (24), applying Stokes' second approximation for wave speed ($\bar{u}_2 = 0$), as the waves considered were generated in a closed wave flume with no prior information available on $\bar{u}_1$. Fenton (1990) noted that the lack of knowledge about $\bar{u}_1$ introduced minor errors; however, the approach provided sufficient engineering accuracy. Furthermore, the wave speed c is determined using either Equation (23) or (24) after calculating $\bar{U}$ or Q from Equations (33) and (35), respectively. The wave speed relation ($c = \lambda/T$) should not be used directly, as from an inertial frame of reference, the wave period would be slightly Doppler-shifted due to the relative motion to a stationary observer.

The fifth-order Stokes surface elevation equation, centered around the free surface, is expressed as:

$$\begin{aligned}\eta = (1/k)[&\varepsilon \cos kX + \varepsilon^2 B_{22} \cos 2kX \\ &+ \varepsilon^3 B_{31} (\cos kX - \cos 3kX) \\ &+ \varepsilon^4 (B_{42} \cos 2kX + B_{44} \cos 4kX) \\ &+ \varepsilon^5 (-(B_{53} + B_{55}) \cos kX + B_{53} \cos 3kX + B_{55} \cos 5kX)\end{aligned} \tag{37}$$

Where $X = (x - ct)$, c is the wave speed, t is the elapsed time, and x is the position of interest in the wave flume. It is noted that $k(x - ct) = kx - \omega t$.

The Bernoulli's constant R, which will be later used to calculate the mean energy flux of each wave, is written as:

$$R = \left(\frac{g}{k}\right) \left[\frac{1}{2} {C_0}^2 + kd + \varepsilon^2 E_2 + \varepsilon^4 E_4\right] \tag{38}$$

Coefficients with numerical subscripts, such as B, C, D, and E, are all complex hyperbolic functions of (kd). For brevity, the formulas for these coefficients are not presented here but are provided in Appendix 2. Fenton (1985) further presented equations for the fluid velocities and pressure; however, these were excluded since the main concern was to produce the free surface equation for validation purposes and later calculate the wave power for efficiency calculations.

3.2.7 Cnoidal wave theory

The second nonlinear theory considered is the Cnoidal theory, derived to handle waves in shallow water depths. It follows a similar approach to that of Stokes but accounts for finite-depth effects; however, it breaks down in deep water conditions, where the Stokes theory is more suitable for application. A special case of the theory arises when the water depth approaches zero. Under such conditions, the solitary wave is obtained and propagates entirely above the surface (Holthuijsen, 2007).

The theory employs Jacobian elliptic functions with an elliptic modulus (m) deeply embedded in all the formulae. Fenton (1998) presented a formulation incorporating Iwagaki's (1968) approximation, which replaced all explicit moduli with unity while retaining elliptic functions and integrals. This was based on the observation that, for shallow waves, the elliptic modulus values approach unity. The modified approximation improved the agreement of velocity profiles with experimental results and extended the theory's applicability to longer waves ($m \geq 0.96$) without loss in accuracy.

In the limit where m is close to unity, an explicit first-order approximation can be used to calculate the elliptic modulus (m) relative to the Ursel number (Fenton, 1998).

$$\sqrt{\frac{3}{16}\,U_{Ursel}} = \sqrt{m}\,K(m) \tag{39}$$

Where K(m) is the 1st type complete elliptic integral, a function of the modulus m.

The K(m) value is approximated as:

$$\lim_{m\to 1} K(m) \approx \frac{1}{2}\log\left(\frac{16}{1-m}\right) \tag{40}$$

Applying the Iwagaki approximation, Equation (40) can be rewritten in terms of m:

$$m = 1 - 16\exp\left(-\sqrt{\frac{3\,U_{Ursel}}{4}}\right) \tag{41}$$

Equation (41) indicates that the elliptic modulus is a relative measure of nonlinearity to dispersion. Furthermore, for applying the Cnoidal theory, the applicability criteria suggested by Hedges (1995) had a limiting Ursel number of 40, which would result in an approximate modulus value of 0.93. Consequently, the modulus is expected to be greater than 0.93 to justify using the Iwagaki approximation (Fenton, 1998).

Similar to the approach used in the Stokes theory, the Cnoidal theory can be formulated using either Equation (23) or (24), which relate the velocity terms in the two frames, as:

$$\frac{\bar{u}_1}{\sqrt{gd}} + \frac{\bar{U}}{\sqrt{gh}}\left(\frac{h}{d}\right)^{1/2} - \frac{\lambda/d}{T\sqrt{g/d}} = 0 \tag{42}$$

$$\frac{\bar{u}_2}{\sqrt{gd}} + \frac{Q}{\sqrt{gh^3}}\left(\frac{h}{d}\right)^{3/2} - \frac{\lambda/d}{T\sqrt{g/d}} = 0 \tag{43}$$

Where h represents the water depth underneath the wave trough. These equations are used to calculate the elliptic modulus (m) after the higher-order wave number is determined, as described next.

The higher-order wavelength (wave number) can be found using the following equation:

$$\frac{\lambda}{d} = \frac{4\,K(m)}{(3H/d)^{1/2}}\left[1 + \left(\frac{H}{d}\right)\left(\frac{5}{8} - \frac{3}{2}e\right) + \left(\frac{H}{d}\right)^2\left(-\frac{21}{128} + \frac{1}{16}e + \frac{3}{8}e^2\right) + \left(\frac{H}{d}\right)^3\left(\frac{20127}{179200} + \frac{409}{6400}e + \frac{7}{64}e^2 + \frac{1}{16}e^3\right) + \left(\frac{H}{d}\right)^4\left(-\frac{1575087}{28672000} + \frac{1086367}{1792000}e - \frac{2679}{25600}e^2 + \frac{13}{128}e^3 + \frac{3}{128}e^4\right)\right] \tag{44}$$

Where $e = E(m)/K(m)$ is the elliptic integral ratio, E(m) is the 2nd type elliptic integral, and K(m) is the 1st type elliptic integral, all of which are functions of the elliptic modulus (Fenton, 1999).

The depth under the trough (h) can be calculated as:

$$\frac{h}{d} = 1 + \left(\frac{H}{d}\right)(-e) + \left(\frac{H}{d}\right)^2\left(\frac{1}{4}e\right) + \left(\frac{H}{d}\right)^3\left(-\frac{1}{25}e + \frac{1}{4}e^2\right) + \left(\frac{H}{d}\right)^4\left(\frac{573}{2000}e - \frac{57}{400}e^2 + \frac{1}{4}e^3\right) + \left(\frac{H}{d}\right)^5\left(-\frac{302159}{1470000}e + \frac{1779}{2000}e^2 - \frac{123}{400}e^3 + \frac{1}{4}e^4\right) \tag{45}$$

The mean horizontal velocity ($\bar{U}$) can be calculated as:

$$\frac{\bar{U}}{\sqrt{gh}} = 1 + \left(\frac{H}{h}\right)\left(\frac{1}{2} - e\right) + \left(\frac{H}{h}\right)^2\left(-\frac{3}{20} + \frac{5}{12}e\right)$$
$$+ \left(\frac{H}{h}\right)^3\left(\frac{3}{56} - \frac{19}{600}e\right) + \left(\frac{H}{h}\right)^4\left(-\frac{309}{5600} + \frac{3719}{21000}e\right) + \left(\frac{H}{h}\right)^5\left(\frac{12237}{616000} - \frac{997699}{8820000}e\right) \quad (46)$$

Finally, the volumetric flow rate per unit width (Q) is given by:

$$\frac{Q}{\sqrt{gh^3}} = 1 + \left(\frac{1}{2}\right)\left(\frac{H}{h}\right) - \left(\frac{3}{20}\right)\left(\frac{H}{h}\right)^2 + \left(\frac{3}{56}\right)\left(\frac{H}{h}\right)^3 - \left(\frac{309}{5600}\right)\left(\frac{H}{h}\right)^4 + \left(\frac{12237}{616000}\right)\left(\frac{H}{h}\right)^5 \quad (47)$$

Substituting Equations (44) through (47) into Equations (42) and (43), two relations are obtained in terms of the elliptic modulus. Depending on whether $\bar{u}_1$ or $\bar{u}_2$ is known, the relations can be numerically solved for the modulus. The bisection method with the bracketing values 0.5, and $1 - 10^{-12}$ can be used to reach a final value (Fenton, 1990). Upon calculating the elliptic modulus, all other values can be calculated using the foregoing equations, and the wave speed can be found using the values of $\bar{U}$ or Q/d, in Equations (23) and (24). The free surface elevation equation, centered around the free surface, is expressed as:

$$\eta - d = h\left[1 + \left(\frac{H}{h}\right)cn\hat{x}^2 + \left(\frac{H}{h}\right)^2\left(-\frac{3}{4}cn\hat{x}^2 + \frac{3}{4}cn\hat{x}^4\right)\right.$$
$$+ \left(\frac{H}{h}\right)^3\left(\frac{5}{8}cn\hat{x}^2 - \frac{151}{80}cn\hat{x}^4 + \frac{101}{80}cn\hat{x}^6\right)$$
$$+ \left(\frac{H}{h}\right)^4\left(-\frac{8209}{6000}cn\hat{x}^2 + \frac{11641}{3000}cn\hat{x}^4 - \frac{112393}{24000}cn\hat{x}^6 + \frac{17367}{8000}cn\hat{x}^8\right) \quad (48)$$
$$+ \left(\frac{H}{h}\right)^5\left(\frac{364671}{196000}cn\hat{x}^2 - \frac{2920931}{392000}cn\hat{x}^4\right.$$
$$\left.\left. + \frac{2001361}{156800}cn\hat{x}^6 - \frac{17906339}{1568000}cn\hat{x}^8 + \frac{1331817}{313600}cn\hat{x}^{10}\right)\right]$$

Here $cn\hat{x}^i = [cn(\hat{x})]^i$, with $\hat{x} = (\alpha\,(x - ct)/h\,,\ m)$, where c is the wave speed, t is the elapsed time, and x is the position of interest within the wave flume, m is the elliptic modulus, and α is the shallowness parameter, defined as:

$$\alpha = \left(\frac{3H}{4h}\right)^{1/2}\left[1 - \frac{5}{8}\left(\frac{H}{h}\right) + \frac{71}{128}\left(\frac{H}{h}\right)^2 - \frac{100627}{179200}\left(\frac{H}{h}\right)^3 + \frac{16259737}{28672000}\left(\frac{H}{h}\right)^4\right] \quad (49)$$

Finally, the Bernoulli's constant is given by:

$$R = gh\left[\frac{3}{2} + \left(\frac{1}{2}\right)\left(\frac{H}{h}\right) - \left(\frac{1}{40}\right)\left(\frac{H}{h}\right)^2 - \left(\frac{3}{40}\right)\left(\frac{H}{h}\right)^3 - \left(\frac{3}{175}\right)\left(\frac{H}{h}\right)^4 - \left(\frac{2427}{154000}\right)\left(\frac{H}{h}\right)^5\right] \quad (50)$$

It is noted that the elliptic integrals and functions $E(m)$, $K(m)$, and cn($\hat{x}$) are embedded in many programming languages, such as MATLAB, and can be calculated automatically. Nonetheless, Fenton (1990) presented approximations suitable for an elliptic modulus value of 0.5 or higher, which are not included here for brevity.

3.2.8 Integral wave properties

Having formulated the wave theories, the auxiliary formulation necessary for calculating integral wave properties can now be presented. The fifth-order Stokes theory approximation for the mean potential energy is given as:

$$V_{pot} = \frac{1}{16}\,\rho g H^2\left(1 + \varepsilon^2\left(2B_{31} + {B_{22}}^2\right)\right) \quad (51)$$

While for the fifth-order Cnoidal theory, the following formula is given:

$$V_{pot} = \rho g H^2\left[\frac{e}{3} - \frac{e^2}{2} + \left(\frac{H}{h}\right)\left(-\frac{e}{10} + \frac{e^2}{4}\right) + \left(\frac{H}{h}\right)^2\left(\frac{9}{2800}e - \frac{57}{800}e^2\right) + \left(\frac{H}{h}\right)^3\left(-\frac{4369}{42000}e + \frac{593}{2000}e^2\right)\right] \quad (52)$$

The formulae are based on corrections introduced by Klopman (1990) but are presented here using the notation of Fenton (1990). All quantities provided are averaged over one wavelength and formulated per unit width in the crest direction.

The mean momentum is given as:

$$I = \rho(cd - Q) \tag{53}$$

Stokes' second approximation of wave speed ($\bar{u}_2 = 0$) results in zero mean wave momentum and a negative mean current ($\bar{u}_1 < 0$). This condition applies to flume-generated waves, which is the case in this study.

The mean kinetic energy is given as:

$$T_{kin} = \frac{1}{2}\rho(\, cI - \bar{u}_1 Q) \tag{54}$$

Where $\bar{u}_1$ can be approximated from the formulations given for each theory.

The mean square of bed velocity is given as:

$$\bar{u}_b{}^2 = 2(R - gd) - c(c - 2\bar{u}_1) \tag{55}$$

Finally, the mean energy flux in [W/m] is:

$$F = c\big(3T_{kin} - 2V_{pot}\big) + \frac{1}{2}\bar{u}_b{}^2(I + \rho cd) - 2c\bar{u}_1 I \tag{56}$$

The mean wave power is calculated by multiplying F by the width of the rotor (0.3 m), yielding the following result:

$$P_{th} = 0.3\, F \tag{57}$$

3.3 Rotor-Free Numerical Wave Flume Model

3.3.1 Model description and governing equation

To further validate the flume-generated waves, a simple rotor-free numerical wave flume (NWF) model was developed using the CFD software Ansys Fluent. The wave flume was modeled in 2D space since the width-to-length ratio of the wave flume was low (0.015), with no cross flow. The numerical modeling of the rotor itself was deemed out of scope under the current study. It was not included in the numerical model due to the limited computational power and to avoid complex fluid-solid interactions. Consequently, optimization simulations were left out for future studies.

The schematic representation of the NWF model is depicted in Figure 3.16. The study region is where the generated wave becomes fully developed. Meanwhile, the damping region employed a numerical beach to prevent wave reflections at the outlet boundary.

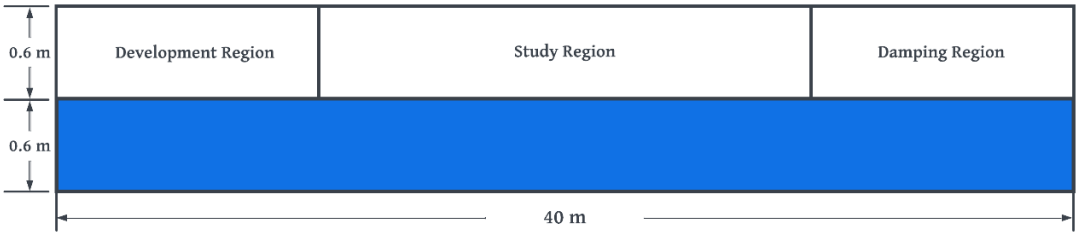

Figure 3.16 Schematical representation of the numerical wave flume model

The simulations employed a finite-volume-based (FVM) discretization method along with a multiphase volume-of-fluid-based (VOF) open channel and wave boundary conditions. Turbulence was accounted for using the shear-stress-transport-based (SST) k-ω model under the assumptions of incompressible, transient, viscous flow conditions, including the effects of gravity as the restoring force. The problem was governed by the continuity and RANS momentum equations.

The formulation involved decomposing instantaneous variables into a time-averaged value plus a fluctuating component (e.g., $u_i = \bar{u}_i + u_i'$). The governing equations utilized in the model are presented in Cartesian tensor notation, omitting the overbar for simplicity, as retrieved from the Ansys Fluent theory guide (ANSYS Inc., 2021).

Firstly, the continuity equation is written as:

$$\frac{\partial \rho}{\partial t} + \frac{\partial}{\partial x_i}(\rho u_i) = 0 \tag{58}$$

Since the flow was assumed incompressible, Equation (58) is rewritten as:

$$\frac{\partial u_i}{\partial x_i} = 0 \tag{59}$$

Where in a two-dimensional model, the velocity term is expressed as:

$$\frac{\partial u_i}{\partial x_i} = \frac{\partial v_x}{\partial x} + \frac{\partial v_y}{\partial y} \tag{60}$$

That is, the divergence of velocity is equal to zero.

As a standard practice in tensor notation, it is noted that when a subscript appears twice, the term is treated as a dummy index, and the components are summed over. A dummy index can be freely relabeled to any subscript of choice (e.g., i, k, l), and hence:

$$\frac{\partial u_i}{\partial x_i} = \frac{\partial u_l}{\partial x_l} = \frac{\partial u_k}{\partial x_k} = \frac{\partial v_x}{\partial x} + \frac{\partial v_y}{\partial y} = 0 \tag{61}$$

Secondly, the RANS momentum equation can be written as:

$$\rho \frac{\partial u_i}{\partial t} + \rho u_j \frac{\partial u_i}{\partial x_j} = -\frac{\partial P}{\partial x_i} + \frac{\partial}{\partial x_j}\left[\mu\left(\frac{\partial u_i}{\partial x_j} + \frac{\partial u_j}{\partial x_i} - \frac{2}{3}\delta_{ij}\frac{\partial u_l}{\partial x_l}\right)\right] + \frac{\partial}{\partial x_j}\left(-\rho\overline{u_i' u_j'}\right) + \rho g_i \tag{62}$$

Noting that $(\partial u_l/\partial x_l = 0)$, from continuity, Equation (62) can be rewritten as:

$$\rho\frac{\partial u_i}{\partial t} + \rho u_j\ \frac{\partial u_i}{\partial x_j} = -\ \frac{\partial P}{\partial x_i} + \ \frac{\partial}{\partial x_j}\left[\mu\left(\frac{\partial u_i}{\partial x_j} + \frac{\partial u_j}{\partial x_i}\right)\right] + \frac{\partial}{\partial x_j}\left(-\ \rho\overline{u_i' u_j'}\right) + \rho g_i \tag{63}$$

Where the term $\left(-\rho\overline{u_i' u_j'}\right)$ is the Reynolds stress tensor, which must be modeled for closure of the numerical model. Utilizing the Boussinesq hypothesis, the following expression is written (ANSYS Inc., 2021):

$$-\ \rho\overline{u_i' u_j'} = \mu_t\left(\frac{\partial u_i}{\partial x_j} + \frac{\partial u_j}{\partial x_i}\right) - \frac{2}{3}\left(\rho k + \mu_t\frac{\partial u_k}{\partial x_k}\right)\delta_{ij} \tag{64}$$

Where the term δ_{ij} is the Kronecker delta, used in the tensor notation to merge the normal and shear stress terms into one equation, and is given as:

$$\delta_{ij} = \begin{cases} 1, & i = j \\ 0, & i \neq j \end{cases} \tag{65}$$

Again, noting that $(\partial u_k/\partial x_k = 0)$ from continuity, Equation (64) can be rewritten as:

$$-\ \rho\overline{u_i' u_j'} = \mu_t\left(\frac{\partial u_i}{\partial x_j} + \frac{\partial u_j}{\partial x_i}\right) - \frac{2}{3}\rho k\delta_{ij} = 2\mu_t S_{ij} - \frac{2}{3}\rho k\delta_{ij} \tag{66}$$

Where S_{ij} is the time-averaged strain tensor, defined as:

$$S_{ij} = \frac{1}{2}\left(\frac{\partial u_i}{\partial x_j} + \frac{\partial u_j}{\partial x_i}\right) \tag{67}$$

Consequently, the RANS momentum equation is rewritten as:

$$\rho\frac{\partial u_i}{\partial t} + \rho u_j\ \frac{\partial u_i}{\partial x_j} = -\ \frac{\partial P}{\partial x_i} + \ \frac{\partial}{\partial x_j}\left[2S_{ij}(\mu + \mu_t) - \frac{2}{3}\rho k\delta_{ij}\right] + \rho g_i \tag{68}$$

Two more equations are required for the closure of the model. These are introduced through the turbulence model and are used to calculate turbulent kinetic energy and specific dissipation rate (ANSYS Inc., 2021).

$$\rho \frac{\partial k}{\partial t} + \rho u_i \frac{\partial k}{\partial x_i} = \frac{\partial}{\partial x_j}\left[\left(\mu + \frac{\mu_t}{\sigma_k}\right)\frac{\partial k}{\partial x_j}\right] + \left(-\rho\overline{u_i' u_j'}\right)\frac{\partial u_j}{\partial x_i} - Y_k + G_b \tag{69}$$

$$\rho \frac{\partial \omega}{\partial t} + \rho u_i \frac{\partial \omega}{\partial x_i} = \frac{\partial}{\partial x_j}\left[\left(\mu + \frac{\mu_t}{\sigma_\omega}\right)\frac{\partial \omega}{\partial x_j}\right] + \frac{\alpha\alpha^*}{\nu_t}\left(-\rho\overline{u_i' u_j'}\right)\frac{\partial u_j}{\partial x_i} - Y_\omega + D_\omega + G_{\omega b} \tag{70}$$

Substituting the previous relations into Equations (69) and (70) results in:

$$\rho \frac{\partial k}{\partial t} + \rho u_i \frac{\partial k}{\partial x_i} = \frac{\partial}{\partial x_j}\left[\left(\mu + \frac{\mu_t}{\sigma_k}\right)\frac{\partial k}{\partial x_j}\right] + \frac{\partial u_j}{\partial x_i}\left[2\mu_t S_{ij} - \frac{2}{3}\rho k \delta_{ij}\right] - Y_k + G_b \tag{71}$$

$$\rho \frac{\partial \omega}{\partial t} + \rho u_i \frac{\partial \omega}{\partial x_i} = \frac{\partial}{\partial x_j}\left[\left(\mu + \frac{\mu_t}{\sigma_\omega}\right)\frac{\partial \omega}{\partial x_j}\right] + \frac{\alpha\alpha^*}{\nu_t}\frac{\partial u_j}{\partial x_i}\left[2\mu_t S_{ij} - \frac{2}{3}\rho k \delta_{ij}\right] - Y_\omega + D_\omega + G_{\omega b} \tag{72}$$

Where Y_k and Y_ω are dissipation effect terms, G_b and $G_{\omega b}$ are buoyancy effect terms, D_ω is the cross-diffusion effect term, σ_k and σ_ω are turbulent Prandtl numbers, ν_t is the kinematic eddy viscosity, and α and $\alpha^*$are model constants. These terms are internally calculated based on the model's constants and are not shown here for brevity.

The turbulent (eddy) viscosity μ_t can be expressed as:

$$\mu_t = \rho \nu_t = \frac{\rho k}{\omega}\left[max\left(\frac{1}{\alpha^*}, \frac{SF_2}{a_1 \omega}\right)\right]^{-1} \tag{73}$$

Where S is the strain rate magnitude, F_2 is a blending relation, and a_1 is a constant. Again, these terms are internally calculated parameters, not shown here for brevity.

The multiphase interaction between phases is tracked using the VOF model through the volume fraction (f), which must add up to unity in all control volumes. Fluid properties are shared according to the volume fractions (ANSYS Inc., 2021).

The VOF-adjusted continuity equation of the water phase (q) can be written as:

$$\frac{1}{\rho_q}\left[\frac{\partial}{\partial t}(f_q\rho_q) + \nabla\cdot(f_q\rho_q u_i) = \sum_{p=1}^{n}(\dot{m}_{pq} - \dot{m}_{qp})\right] \tag{74}$$

While the volume fraction of the primary air phase is computed from:

$$\sum_{q=1}^{n} f_q = 1 \rightarrow\ f_p = 1 - f_q \tag{75}$$

Since the phases are immiscible and incompressible, Equation (74) can be rewritten as:

$$\frac{\partial f_q}{\partial t} + \frac{\partial}{\partial x_i}(f_q u_i) = 0 \tag{76}$$

Other fluid properties in the computational domain are determined depending on the volume fractions. For example, the density in each control volume is given as:

$$\rho = \sum_{q=1}^{n} f_q\rho_q \rightarrow \rho = f_q\rho_q + (1 - f_q)\rho_p \tag{77}$$

Similar expressions can be written for all other properties, including viscosity. The RANS momentum equation remains unchanged, and the velocity is shared between phases according to volume fractions. Finally, numerical reflections from the flume's outlet are reduced using a momentum sink term (Liu et al., 2018; ANSYS Inc., 2021), as follows:

$$S_{sink} = -\left[C_1\rho V + \frac{1}{2}C_2\rho|V|V\right]f(y)f(x) \tag{78}$$

$$f(x) = \left(\frac{x - x_s}{x_e - x_s}\right)^2 \tag{79}$$

$$f(y) = 1 - \left(\frac{y - y_{fs}}{y_b - y_{fs}}\right) \tag{80}$$

Where S_{sink} is the momentum sink term, C_1 and C_2 are special and temporal damping resistances, V is the vertical velocity term, and x_s, x_e, y_{fs}, and y_b represent the start, end, free surface, and bottom levels of the damping zone.

3.3.2 Numerical flume geometry and meshing

The wave flume was modeled in 2D space to simplify the analysis, with the dimensions depicted in Figure 3.16. The model was recreated in the Design Modeler of ANSYS Fluent, as illustrated in Figure 3.17, where the origin point was positioned at the center of the flume, equidistant at 20 meters from the inlet and outlet and 0.6 meters from both the bottom and top of the tank.

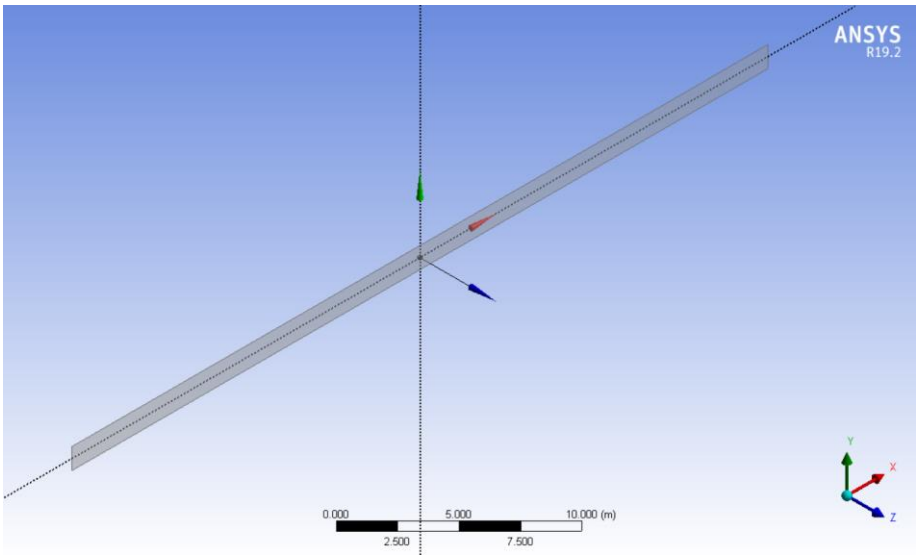

Figure 3.17 The numerical wave flume geometry in Design Modeler

To ensure a good resolution in the domain, the number of computational mesh elements in the wave amplitude orientation should be set between 10 to 20 cells, which could be computationally demanding depending on wave characteristics (ANSYS Inc., 2021). In that regard various meshes were tested to optimize the required computational power

and simulation time, while maintaining good resolution. Specifically, three meshes were tested and are presented in Table 3.3.

Table 3.3 The various meshes used for the mesh independency analysis

Mesh No.	Nodes	Elements	Vertical Divisions	Horizontal Divisions	Element Size
1	20025	19200	24	800	5 cm
2	122061	120000	60	2000	2 cm
3	484121	480000	120	4000	1 cm

An automatic all-quad paved multizone quad/tri meshing approach was inserted to optimize the time required to complete the mesh. Furthermore, an edge sizing technique was followed using the vertical and horizontal number of divisions shown in Table 3.3. The number of divisions is calculated according to the dimensions of the flume and the required element size. For example, if an element size of 1 cm is required, then the 120 cm vertical inlet of the flume should be divided into 120 segments. Finally, named selections are created for the boundaries as depicted in Figure 3.18.

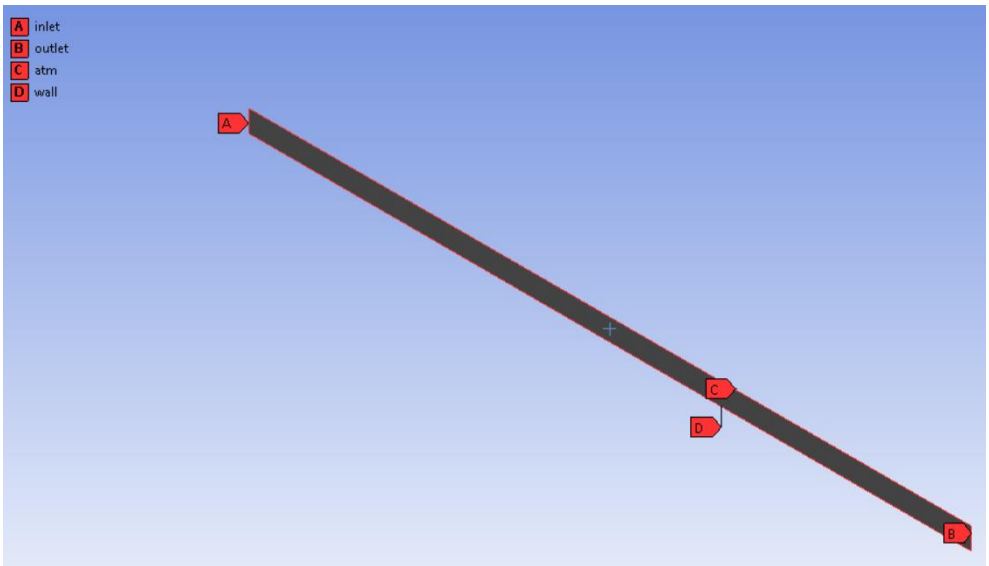

Figure 3.18 The named selections for the boundary conditions used in the model

3.3.3 Solver settings and solution methods

The solvers (pressure- or density-based) of Ansys Fluent utilize the FVM to process the governing equations. The domain is subdivided into smaller control volumes, where differential equations are discretized into linearized algebraic relations and solved iteratively. The pressure solver is utilized for simulations involving incompressible fluids, while the density solver is more suitable for compressible fluid flow simulations. The density solver calculates density from continuity and pressure fields using a state equation. In contrast, the pressure solver determines pressure using continuity and momentum equations. Regardless of the solver, the velocity field is always calculated from the momentum equation (ANSYS Inc., 2021).

The numerical model assumes incompressible, transient, viscous, and two-dimensional. Consequently, the planar, absolute, transient pressure-based solver was employed with active vertical gravity. Moreover, the air-water interface was modeled using sharp, implicit volume of fluid (VOF) multiphase model with active copen channel and wave boundary conditions (Khaware et al., 2018). Finally, due to its accuracy under various flow conditions, the SST k-ω viscous model with turbulence damping was utilized to model turbulence (Windt et al., 2018; Ringe, 2020; ANSYS Inc., 2021).

The numerical wave flume (NWF) boundary conditions were set as velocity inlet at the wave generation boundary, pressure outlet at the wave outlet and the upper boundaries, and wall at the bottom boundary, with open channel wave boundary conditions activated. The related wave heights, wavelengths, free surface, and bottom level were defined in the velocity inlet condition together with a suitable wave theory. A numerical beach was defined in the cell zone conditions to prevent wave reflections (Connell & Cashman, 2016; Arabic CFD, 2020).

Additionally, a pressure-implicit splitting-of-operators-based (PISO) scheme was used for the P-V coupling to enhance convergence. The scheme incorporates skewness-neighbour corrections, effectively reducing the total number of iterations required for convergence while maintaining robust accuracy, even in complex or highly skewed computational meshes. The least-squares cell-based scheme was used for spatial discretization, while the pressure-staggering-option was utilized to interpolate pressure. The 2^{nd} order upwind method was applied to calculate momentum and capture flow gradients, and the modified HRIC method was used to track the volume fraction between phases. The 1^{st} order upwind method ensured numerical stability for k and ω. Lastly, the bounded 2^{nd} order implicit formulation was utilized for the time formulation, with the step size determined by dividing the wave period by 100, as recommended in the literature (Barton, 1998; Khaware et al., 2018; ANSYS Inc., 2021). It is noted, however, that for larger wave periods, convergence issues may be encountered and can be overcome with a finer time step size, such as 0.01 s.

Details of the numerical formulations of the above computational schemes and solver settings were omitted for the present discussion for brevity, with further information available in the theory guide of Ansys Fluent (ANSYS Inc., 2021).

3.3.4 Numerical wave conditions and theory suitability

Ansys Fluent can assess the suitability of the selected wave theory at the velocity inlet according to other input parameters. As outlined in the theoretical model, the Stokes wave theory applies to waves with finite amplitudes in intermediate-to-deep water depths. In contrast, the Cnoidal wave theory is ideal for waves with flatter troughs and narrower crests in shallower water depths. Both wave theories in Fluent are formulated based on J. D. Fenton's work, forming the foundation of this study's theoretical model. The numerical formulations of these theories are not presented here for brevity.

Nonlinear effects increase with increasing wave steepness. Regular, stable nonlinear waves should maintain a single crest without secondary crest formations at their troughs, as illustrated in Figure 3.19. This instability is commonly observed in second- and fourth-order nonlinear wave theories. The software's numerical stability criteria for monitoring these wave parameters are discussed next (Koo, 2004; ANSYS Inc., 2021).

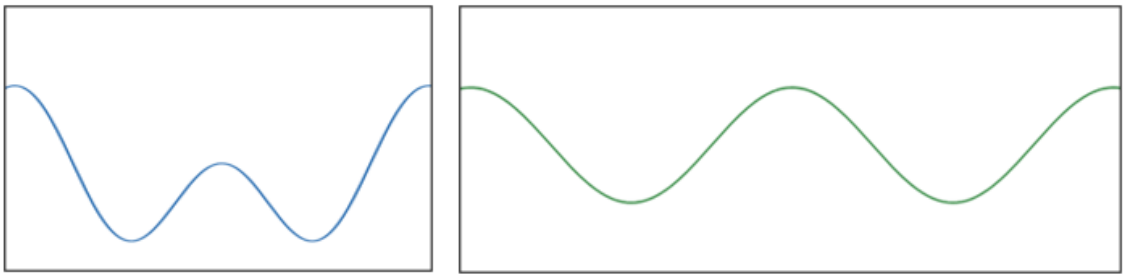

Figure 3.19 Comparison of multi-crest wave distortion (left) and a regular wave (right)

The following limiting values, outlined in the Ansys Fluent theory guide, should be considered to determine the suitability of the wave theory according to input parameters defined at the inlet wave boundary condition. These parameters include wave height, wavelength, and bottom/free levels (ANSYS Inc., 2021). Specifically, the height-to-depth and height-to-wavelength ratios must remain within the breaking limits, such that:

$$\begin{aligned} &Maximum\ Theoretical\ Limits: && \frac{H}{d} \leq 0.78 && \frac{H}{\lambda} \leq 0.142 \\ &Maximum\ Numerical\ Limits: && \frac{H}{d} \leq 0.55 && \frac{H}{\lambda} \leq 0.12 \end{aligned} \tag{81}$$

Additionally, the depth region is checked to ensure the suitability of the selected theory.

$$\frac{d}{\lambda} \begin{cases} \geq 0.5 & Short\ gravity\ waves\ (Linear) \\ \geq 0.06 & Stokes\ waves \\ \leq 0.085 & Shallow\ waves \end{cases} \tag{82}$$

Similarly, the wave steepness and relative wave height are checked as follows:

$$\frac{H}{\lambda} \begin{cases} \leq 0.02\ tanh\left(2\pi\frac{d}{\lambda}\right) & Linear\ waves \\ \leq 0.142\ tanh\left(2\pi\frac{d}{\lambda}\right) & Stokes\ waves \\ \leq 0.142\left(2\pi\frac{d}{\lambda}\right) & Shallow\ waves \end{cases} \tag{83}$$

$$\frac{H}{d} \begin{cases} \leq 0.1 & Linear\ waves \\ \leq 0.5 & Stokes\ waves \\ \leq 0.55 & Shallow\ waves \end{cases} \tag{84}$$

Finally, the Ursel number (nonlinearity measure) is checked as follows:

$$Ur = \frac{H\lambda^2}{d^3} \begin{cases} \leq \frac{32\pi^2}{3} & Linear\ waves \\ \leq \frac{8\pi^2}{3} & Stokes\ waves \\ \geq \frac{8\pi^2}{3} & Shallow\ waves \end{cases} \tag{85}$$

Stokes waves are stable in simulations when their relative heights (H/d) are less than 0.4, the steepness (H/λ) is below 0.1, and the Ursell number is below 10. If these values increase, the waves may break unless the selected wave theory is adjusted to account for the changes. In the transitional ranges, where steepness (H/λ) is between 0.1 and 0.12, and the Ursell number is between 10 and 26, the numerical results can become less reliable, and stability is more challenging to maintain. (ANSYS Inc., 2021).

To automatically verify applicability of a wave theory based on the foregoing criteria, the following command should be entered in the command window of the software upon defining the inlet wave boundary condition, but before initializing or running the simulation: (*define/boundary-condition/open-channel-wave-setting*). The program will then assess whether the selected wave theory is appropriate for the input wave parameters. A sample check is shown in Figure 3.20. It should be noted that the symbol (h) stands for depth in the software's notation, which corresponds to (d) in the notation used in the above discussion (ANSYS Inc., 2021).

```
define/boundary-condition/open-channel-wave-setting

Wave Input Analysis for Velocity Inlet : Thread ID = 5
************************************************************

Wave-1 Analysis
****************************************

Current Settings :
------------------
Wave theory : 5th-order-Stokes , Wave regime = Shallow/Intermediate
Wave Height (H) = 0.0500, Wave Length (L) = 1.0120
Liquid Depth (h) = 0.5000, Ursell Number (H*L*L/(h*h*h)) = 0.4097

Mandatory checks for full wave regime within wave breaking limit
----------------------------------------------------------------
Relative Height: H/h = 0.1000 , Maximum theoretical limit = 0.7800
Maximum numerical limit = 0.5500
Relative height within wave breaking limit

Wave Steepness: H/L = 0.0494 , Maximum theoretical limit = 0.1420
Stable numerical limit = 0.1000 , Maximum numerical limit = 0.1200
Wave steepness within wave breaking limit

Checks for selected wave theory within wave breaking and stability limit
------------------------------------------------------------------------
Relative height check
H/h = 0.1000 , Min : 0.0000 , Max : 0.5000
Relative height check : successful

Wave Steepness check
H/L = 0.0494 , Min : 0.0000 , Max : 0.1414
Wave steepness check : successful

Ursell Number check
Ur = 0.4097 , Min : 0.0000 , Max : 25.0000
Ursell number check : successful

Wave regime check
h/L = 0.4941 , Min : 0.0600 , Max : 10000.0000
Wave regime check : successful

Summary
-----------------------
Checks : passed
Selected wave theory is appropriate for application.
```

Figure 3.20 A sample Fluent check for wave theory suitability and numerical stability

3.3.5 Numerical wave power calculation

The approximate power within the numerical flume was calculated for comparison with the theoretical model. Although the wave formulation is the same, Fluent does not provide a direct method for calculating wave energy flux. Instead, an indirect approximate scheme was developed.

The approach involved setting up monitor lines at various locations along the flume before running the simulation, defining integral surface reports to track the water's volume fraction and determine surface elevation. After the wave fully developed, the time lag between data records of two monitors placed at a known distance from one another was used to calculate the wave speed. The group velocity was subsequently estimated, and the wave energy flux was calculated by multiplying the group velocity by the energy density. The equations used are outlined below.

Wave speed was calculated from propagation between two numerical wave gauges as:

$$c_{num} = \frac{\Delta x}{\Delta t} = \frac{x_{gauge\,(2)} - x_{gauge\,(1)}}{t_2 - t_1} \tag{86}$$

Then the mean energy flux per unit crest width in [W/m] was calculated as:

$$F = \left[T_{kin} + V_{pot}\right]\left[\frac{1}{2} c_{numerical}\left(1 + \frac{4\pi d/\lambda_{higher-order}}{sinh\left(4\pi d/\lambda_{higher-order}\right)}\right)\right] \tag{87}$$

4. RESULTS AND DISCUSSION

4.1 Validation Analyses

4.1.1 Experimental wave validation

During the experiments, the upstream surface elevation data of the flume-generated waves were recorded with a wave gauge placed at the 5-m mark from the wave generator. The recorded data is plotted against the theoretical elevation profiles calculated using the Stokes/Cnoidal theories to validate the flume-generated waves. Two surface elevation plots are shown in Figures 4.1 and 4.2 for both theories, respectively.

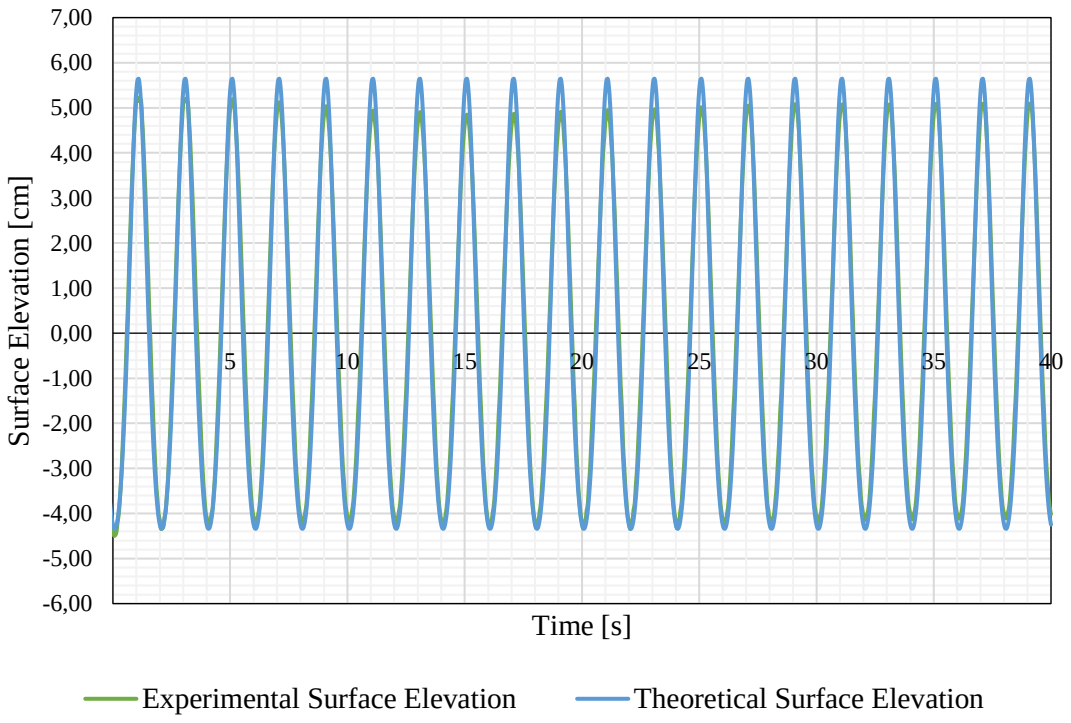

Figure 0.1 Validation plot for the 5th order Stokes theory (H = 10 cm, T = 2 s, x = 5 m)

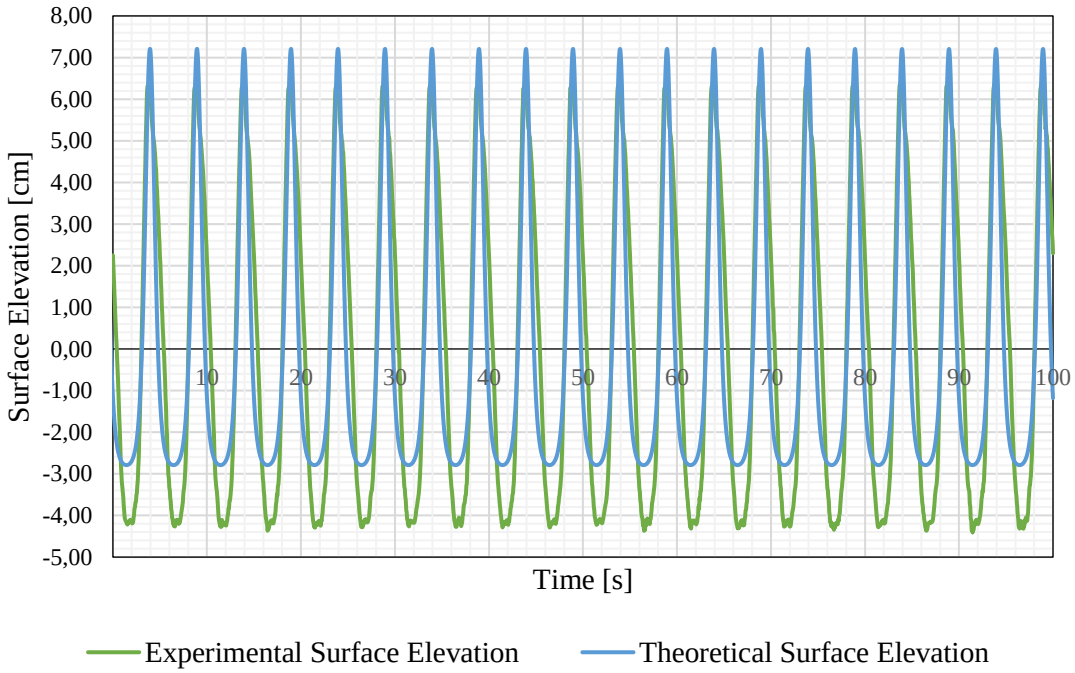

Figure 0.2 Validation plot for the 5th order Cnoidal theory (H = 10 cm, T = 5 s, x = 5 m)

Experimental elevation records from the flume showed close alignment with wave theory, confirming that the incident wave trains were fully developed before reaching the prototype and that the theories are valid. However, minor offsets were observed, particularly for shallow-water waves, as in Figure 4.2. These offsets likely originated from interactions with the flume's boundaries or wave reflections. In wave flumes, even slight wave reflections can cause interference patterns that amplify or diminish wave characteristics (Goda, 2010). Instrumental noise may also amplify these variations, resulting in the observed patterns. These factors help explain the consistent but slightly altered wave profiles. A similar behavior was observed for all wave combinations.

4.1.2 Mesh independence and numerical validation

Three meshes were tested to determine the best surface elevation resolution compared to the theoretical model. The number of elements used, and other mesh details were previously summarized in Table 3.3. The elevation plots depicted below are from initial runs that were performed prior to the full numerical simulation.

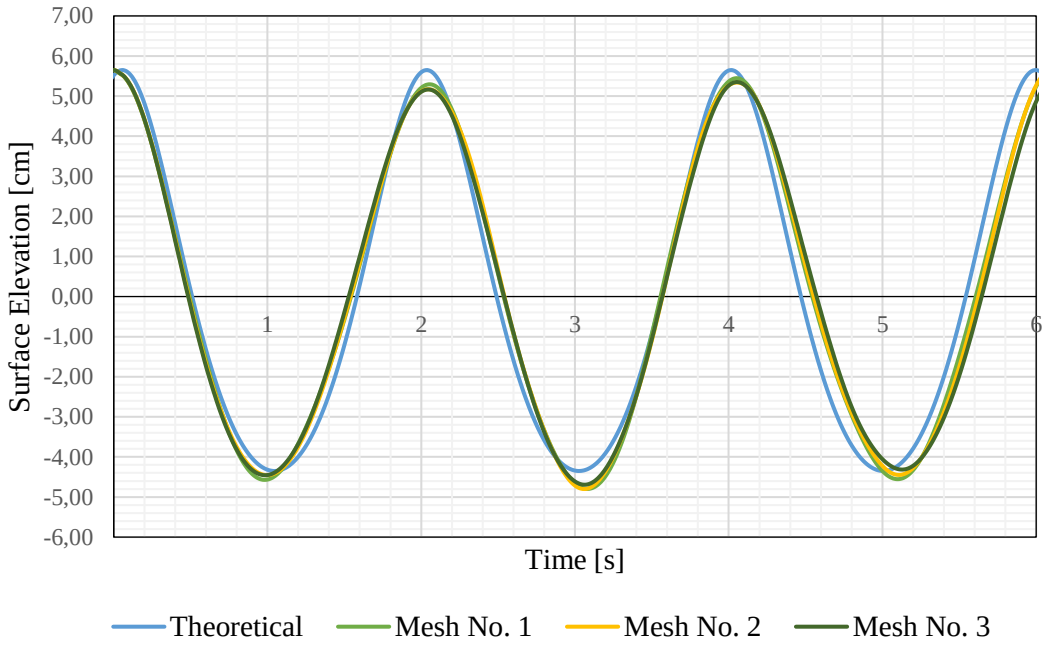

Figure 0.3 Mesh independency wave profile comparison for various meshes

These initial simulation runs indicated that the numerically generated waves were almost all independent of the mesh element size and closely aligned with the theory. However, slight phase shifts were noted between the numerical and theoretical profiles, which probably resulted from viscous effects within the numerical flume, unlike the inviscid assumption of the theory. Consequently, the finest mesh, mesh No. 3, with an element size of 1 mm, was used for subsequent simulations to maintain the highest possible wave profile resolution at a reasonable computational cost and run time.

Similar to the experimental wave generation validation plots against the theory, the NWF-generated waves were compared with experimental and theoretical wave profiles, as shown in Figures 4.4 and 4.5. Again, the plots aligned well with the theory, with slight phase shifts observed mainly caused by boundary interactions and frictional effects. The numerical model was deemed valid for roughly modeling the flume without introducing the rotor within the scope of this study.

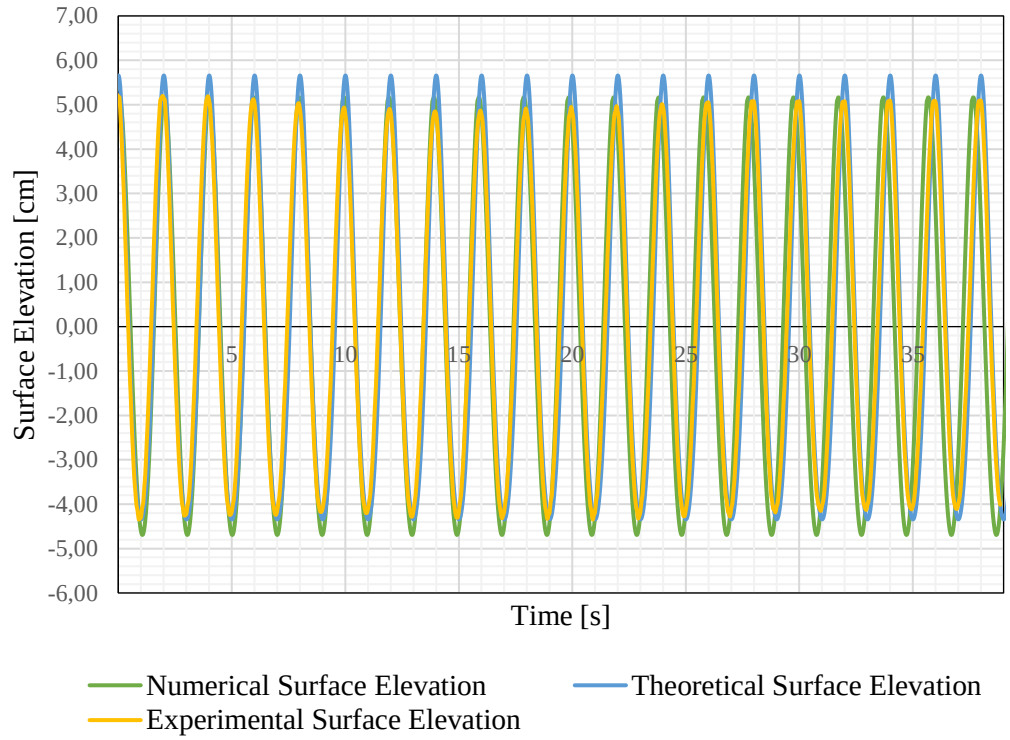

Figure 0.4 Numerical validation plot (H = 10 cm, T = 2 s, x = 5 m)

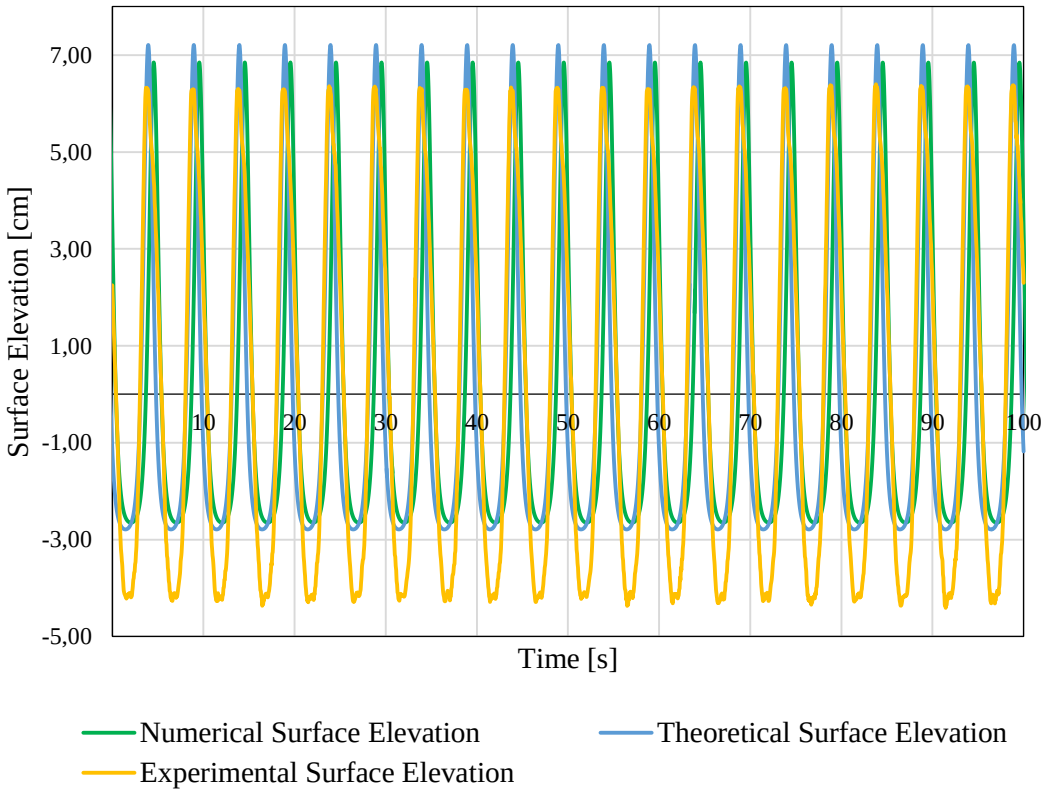

Figure 0.5 Numerical validation plot (H = 10 cm, T = 5 s, x = 5 m)

The above results showed that the flume-generated and model-generated regular gravity surface waves aligned with nonlinear theory introduced in the theoretical model. Thus, the calculated wave power values were accepted as valid for further efficiency calculations to assess the converter's experimental performance in the flume. The wave power calculation results are presented in the following section.

4.1.3 Visualization of the numerical flume

Fluent's VOF representation showing the NWF is given in Figure 4.6. The monitor lines at which the wave profiles were obtained are indicated in the figure. A total of seven monitors were used in this case.

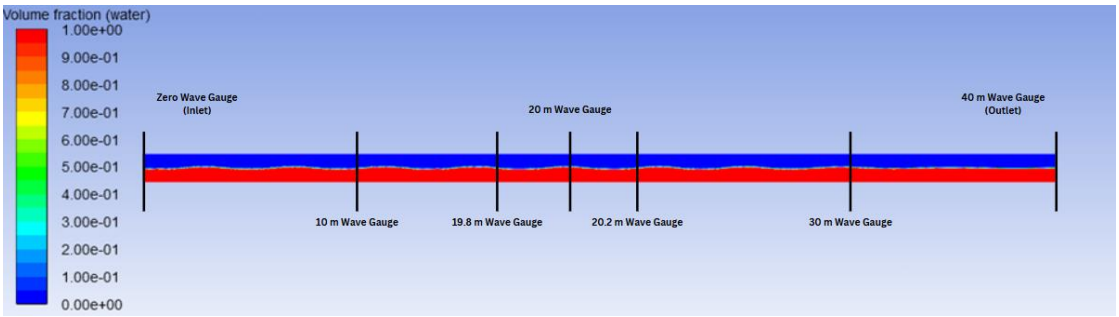

Figure 0.6 The VOF representation of the numerical wave flume

The elevation plot of the inlet's VOF surface monitor line is depicted in Figure 4.7. Initially, the free water surface is horizontal, and as time elapses, the wave profile begins to develop. Convergence is reached after initial iterations to reach numerical stability under the present conditions.

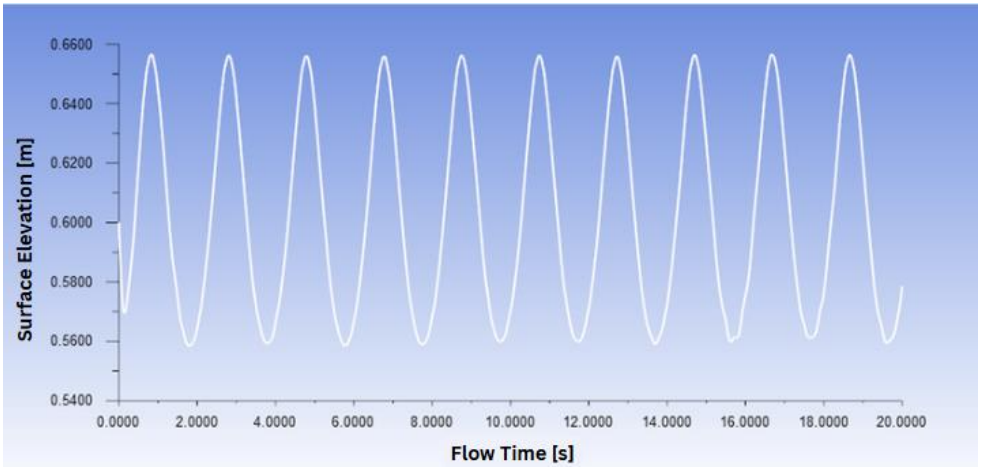

Figure 0.7 The numerical elevation, inlet wave gauge (H = 10 cm, T = 2 s)

The surface elevation plots of the 19.8-m gauge and the 20-m gauge were used to calculate the wave speed of this wave by dividing the distance between them by the time lag in their recorded wave profile data when the recorded profile data was closest to the fully developed plot of Figure 4.7. The phase shift is shown in Figure 4.8.

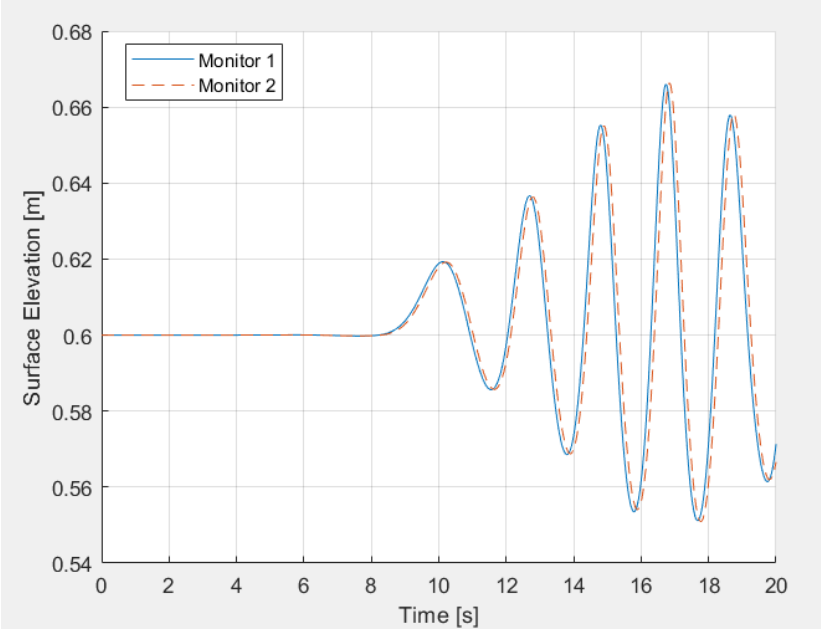

Figure 0.8 Time lag between numerical monitor data for a propagating wave

These visual indications from the CFD software Ansys Fluent indicate a stable numerical model for the present wave flume. However, it is noted that more considerable lengths of the domain may be required for larger waves depending on the damping performance and whether or not wave reflections are occurring.

4.2 Wave Power Calculations

The wave power calculation results of the fifth-order nonlinear Stokes and Cnoidal theories are shown within Table 4.1.

Table 0.1 The fifth-order nonlinear theoretical wave power calculation results

H [cm]	T [s]	λ [m]	Region	Theory	F [W/m]	P [W]
10	2	4.38	Intermediate	Stokes	21.63	6.49
	3	7.03	Intermediate	Stokes	25.13	7.54
	4	13.53	Shallow	Cnoidal	24.20	7.26
	5	12.23	Shallow	Cnoidal	24.68	7.40
20	2	4.45	Intermediate	Stokes	83.55	25.07
	3	7.15	Intermediate	Cnoidal	88.12	26.44
	4	9.99	Intermediate	Cnoidal	90.60	27.18
	5	12.78	Shallow	Cnoidal	84.45	25.34

Similarly, Table 4.2 summarizes the linear theory results for comparison.

Table 0.2 The linear theoretical wave power calculation results

H [cm]	T [s]	λ [m]	Region	E [J/m2]	F [W/m]	P [W]
10	2	4.36	Intermediate	12.26	21.85	6.56
	3	6.95	Intermediate	12.26	25.97	7.79
	4	9.46	Intermediate	12.26	27.57	8.27
	5	11.93	Intermediate	12.26	28.34	8.50
20	2	4.36	Intermediate	49.05	87.39	26.22
	3	6.95	Intermediate	49.05	103.88	31.16
	4	9.46	Intermediate	49.05	110.29	33.09
	5	11.93	Intermediate	49.05	113.36	34.00

When the depth is constant but the wave period/height changes, the depth-to-wavelength ratio adjusts, altering nonlinearity and shifting the depth regimes. This transition reduces the available energy flux, underscoring the importance of nonlinear theories in accurately evaluating wave energy behavior under varying conditions. Nonlinear wave theories account for nonlinear effects, especially in transitional water depth regions. While linear theory is practical for low steepness, it becomes inadequate when its assumptions are violated. Nonlinearity arises as waves transition into shallower waters or increase in height, leading to sharper crests, flatter troughs, and energy

redistribution to higher harmonics, a phenomenon that the linear model cannot accurately capture (Fenton, 1990; Svendsen, 2006). The Ursel number ($H\lambda^2/d^3$) measures nonlinearity and increases significantly for shallow waves. As the Ursel number increases, nonlinear theories incorporating higher-order terms become essential to capture complex interactions. Stokes theory is practical for moderate depth regions, whereas Cnoidal theory better represents shallow water conditions with small depth-to-wavelength (d/λ) ratios (Barthelemy, 2004; Ursell, 1953). These nonlinear effects directly impact energy flux calculations as energy shifts from the primary wave to higher harmonics. Moreover, wave breaking and frictional dissipation decrease the available energy flux in real-life conditions. As a result, nonlinear models provide more conservative estimates than the linear model, which aligns better with the physical nature of the waves (Svendsen, 2006; Barthelemy, 2004). Table 4.3 summarizes the approximate numerical wave power results.

Table 0.3 Approximate numerical wave power calculation results

H [cm]	T [s]	λ [m]	Region	Theory	F [W/m]	P [W]
10	2	4.38	Intermediate	Stokes	22.00	6.60
	3	7.03	Intermediate	Stokes	25.28	7.58
	4	13.53	Shallow	Cnoidal	24.61	7.38
	5	12.23	Shallow	Cnoidal	25.09	7.53
20	2	4.45	Intermediate	Stokes	85.76	25.73
	3	7.15	Intermediate	Cnoidal	92.53	27.76
	4	9.99	Intermediate	Cnoidal	94.26	28.28
	5	12.78	Shallow	Cnoidal	87.60	26.28

As anticipated, the numerical results were similar to their theoretical counterparts. Consequently, the fifth-order nonlinear theoretical wave formulation is used in subsequent conversion efficiency calculations as it is more conservative than the numerical and linear models.

4.3 Experimental Results

4.3.1 Energy conversion performance

Instantaneous net torque and rotational speed data were post-processed to calculate the average net torque, mean power, and efficiency relative to wave theory for each experimental case. Table 4.4 summarizes the experimental results.

Table 0.4 Experimental power analysis results at a water depth of 60 cm

Submergence			Zero Position			-10 cm Position		
T [s]	H [cm]	N_{motor} [RPM]	$\tau_{avg\text{-}net}$ [Nm]	P_{avg} [W]	η	$\tau_{avg\text{-}net}$ [Nm]	P_{avg} [W]	η
2	10	60	0.52	0.33	5.06	0.86	0.54	8.31
		84	0.54	0.47	7.30	0.58	0.51	7.89
		108	0.38	0.43	6.58	0.43	0.48	7.45
	20	60	1.40	0.88	3.51	0.95	0.60	2.39
		84	1.19	1.04	4.17	1.18	1.04	4.13
		108	0.78	0.89	3.53	0.79	0.90	3.58
3	10	40	0.75	0.31	4.16	0.71	0.30	3.93
		56	0.55	0.32	4.25	0.63	0.37	4.90
		72	0.43	0.33	4.33	0.53	0.40	5.26
	20	40	1.58	0.66	2.51	0.77	0.32	1.23
		56	0.86	0.51	1.91	0.91	0.53	2.01
		72	0.75	0.57	2.14	0.80	0.61	2.29
4	10	30	0.87	0.27	3.79	0.52	0.16	2.27
		42	0.43	0.19	2.62	0.41	0.18	2.51
		54	0.36	0.20	2.77	0.37	0.21	2.87
	20	30	1.49	0.47	1.73	1.62	0.51	1.87
		42	1.85	0.82	3.00	1.42	0.63	2.31
		54	1.21	0.68	2.51	1.34	0.76	2.79
5	10	24	0.71	0.18	2.41	0.73	0.18	2.48
		33.6	0.92	0.32	4.36	0.51	0.18	2.42
		43.2	0.39	0.17	2.36	0.44	0.20	2.66
	20	24	0.97	0.24	0.96	0.85	0.21	0.84
		33.6	1.71	0.60	2.37	0.77	0.27	1.06
		43.2	0.73	0.33	1.30	0.70	0.32	1.25

Table 4.4 Experimental power analysis results at a water depth of 60 cm (continued)

Submergence			-15 cm Position			-20 cm Position		
T [s]	H [cm]	N_{motor} [RPM]	$\tau_{avg\text{-}net}$ [Nm]	P_{avg} [W]	η	$\tau_{avg\text{-}net}$ [Nm]	P_{avg} [W]	η
2	10	60	0.33	0.21	3.17	0.20	0.12	1.89
		84	0.27	0.24	3.68	0.06	0.05	0.83
		108	0.13	0.15	2.30	0.04	0.05	0.76
	20	60	1.33	0.84	3.34	1.22	0.76	3.05
		84	0.91	0.80	3.20	0.82	0.72	2.87
		108	0.55	0.62	2.47	0.57	0.65	2.59
3	10	40	0.15	0.06	0.82	0.76	0.32	4.21
		56	0.16	0.09	1.21	0.55	0.32	4.29
		72	0.05	0.03	0.45	0.46	0.34	4.56
	20	40	0.69	0.29	1.09	0.68	0.29	1.08
		56	0.50	0.30	1.12	0.58	0.34	1.28
		72	0.40	0.30	1.13	0.52	0.39	1.49
4	10	30	0.45	0.14	1.94	0.52	0.16	2.25
		42	0.37	0.16	2.24	0.55	0.24	3.30
		54	0.22	0.13	1.75	0.39	0.22	3.07
	20	30	0.73	0.23	0.85	0.90	0.28	1.04
		42	0.58	0.26	0.95	0.88	0.39	1.43
		54	0.50	0.28	1.04	0.73	0.41	1.52
5	10	24	0.46	0.12	1.57	0.50	0.13	1.70
		33.6	0.31	0.11	1.47	0.41	0.15	1.97
		43.2	0.14	0.06	0.86	0.30	0.14	1.82
	20	24	1.07	0.27	1.06	0.65	0.16	0.65
		33.6	0.80	0.28	1.11	0.51	0.18	0.70
		43.2	0.61	0.28	1.09	0.35	0.16	0.63

The table highlights the parametric combinations used during the experiments and their corresponding experimental power analysis results. As mentioned, the motor's rotational speed was four times that of the rotor. It was set to turn the rotor proportionally to the incident wave frequency at 0.5, 0.7, and 0.9 times its value according to Equation (2). Furthermore, Figure 4.9 depicts a selection of time history plots illustrating the experimental torque and rotational speed data.

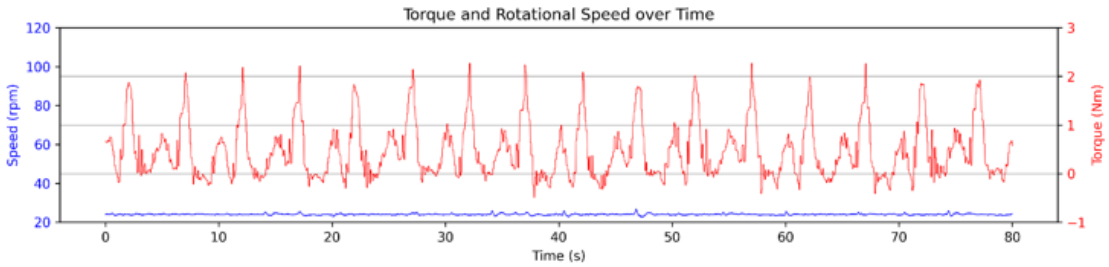

a. Time history at H = 10 cm, T = 5 s, N_{motor} = 24 rpm (0.5 ω), and z = -15 cm (η = 1.57%).

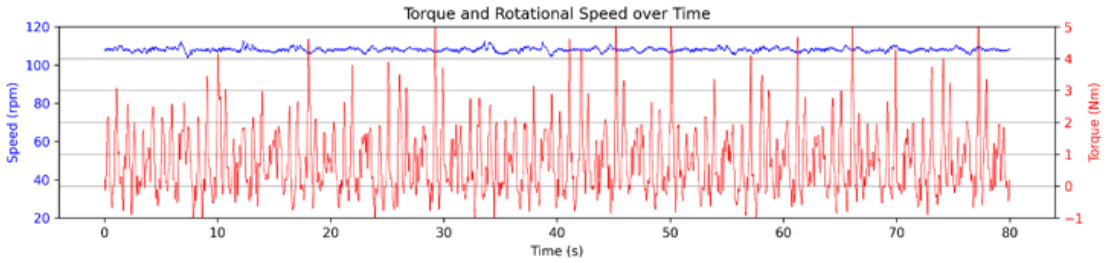

b. Time history at H = 20 cm, T = 2 s, N_{motor} = 108 rpm (0.9 ω), and z = -10 cm (η = 3.58%).

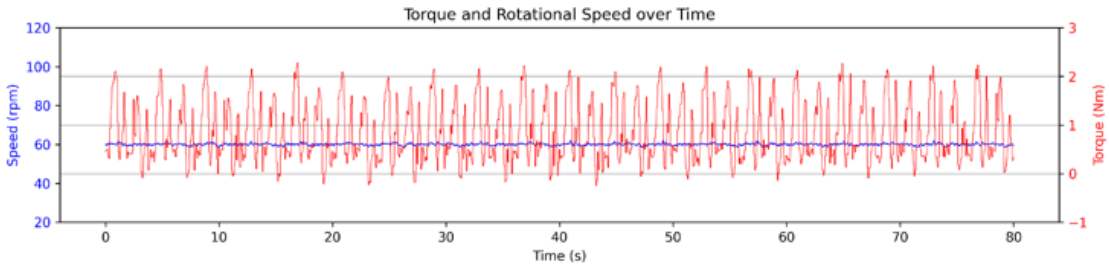

c. Time history at H = 10 cm, T = 2 s, N_{motor} = 60 rpm (0.5 ω), and z = -10 cm (η = 8.31%).

Figure 0.9 Records of selected instantaneous torque and rotational speed data

Over time, the instantaneous torque and rotational speed records indicated a net wave-induced torsional effect acting on the rotor due to the predominantly positive net torque. Furthermore, the rotational speed remained stable overall, with only minor fluctuations within acceptable limits bounding the motor's initial set values calculated relative to the wave period. As intended, the system's bulk rotation was consistently unidirectional, with the servo motor adjusting its output to maintain the desired speed. Finally, Figure 4.9 suggests that the prototype's ability to capture the wave-induced torque decreases when less frequent waves (larger wave periods) were considered.

4.3.2 Experimental observations and data visualization

The performance of the present converter was analyzed by examining how different experimental parameters affect conversion efficiency. These parameters included combinations of wave heights and periods at various submergence levels and rotational speeds, which defined the experimental conditions summarized in Table 4.4. The experimental efficiency values are visualized using the heat map plot shown below.

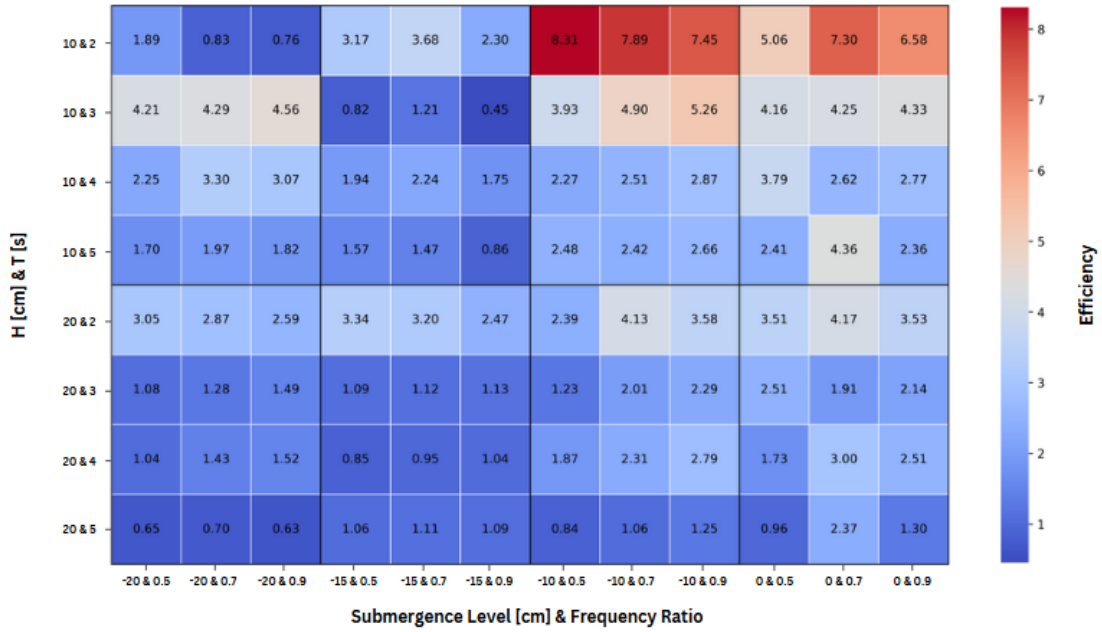

Figure 0.10 Heat map visualization of the experimental efficiency values

The analysis examined the relationship between wave parameters and the conversion efficiency of the rotor system. It focused on how variations in wave height, period, and submergence influenced performance under the current experimental configuration. Particular attention was given to efficiency trends and the stability of wave-rotor interactions. The findings provide insights into optimal operating conditions for maximizing wave energy conversion.

Figure 4.5 demonstrates that, for most experimental cases, an increase in wave height at constant period was associated with reduced conversion efficiencies, regardless of the rotor's submergence level or rotational speed. Although the energy flux available for conversion increased with wave height, the observed decline in efficiency indicated that the wave-rotor interaction was more stable under smaller wave heights at the present scale and configuration, while larger waves overwhelmed the system, resulting in instabilities that adversely affected performance. In contrast, efficiency enhancements were observed at lower wave periods, as increasing the wave period resulted in less frequent rotor-wave interaction, consistent with findings in the literature (Faizal et al., 2009; Ahmed et al., 2010; Ahmed et al., 2013; Hindasageri et al., 2011).

Rotational speed was dictated by the wave period proportional to the wave's angular frequency; however, no consistent patterns regarding the frequency ratio were observed, indicating that it did not affect efficiency as much as expected. Nevertheless, rotational speed control was necessary to facilitate the dynamic torque measurement technique in the present study, as a mechanical counter load was required to record a net torque output signal. Finally, higher efficiency values were observed closer to the free surface, particularly at a -10 cm submergence. This behavior was expected due to the larger particle orbits and, consequently, higher kinetic energy near the water surface (Faizal et al., 2009; Ahmed et al., 2010; Ahmed et al., 2013; Hindasageri et al., 2011).

Optimal performance was observed at a submergence level of -10 cm below the mean water surface, with a rotational frequency ratio 50% of the incident wave's angular frequency, under a wave height and period of 10 cm and 2 s, respectively (Stokes wave).

4.4 Deep Learning Data Analysis

4.4.1 Data pre-processing and rationale

In addition to the experimental findings, a deep-learning neural network-based model was created to investigate the sensitivity of conversion efficiency to the operational parameters. Deep learning was used to model data and find hidden patterns, overcoming the limits of traditional regression methods (Kyriazos & Poga, 2024). The input dataset included wave height, wave period, frequency ratio, and submergence level. Categorical inputs (frequency ratio and submergence) were transformed into binary values using the One-Hot Encoding method, as illustrated in Table 4.5. For instance, if the network reads the input combination 0-0-0-1 and 1-0-0, it translates into a submergence level of -20 cm and a percentage frequency ratio of 50%, respectively. In contrast, continuous variables (height and period) were preprocessed using the Standard Scaler approach to ensure equal feature importance (Haykin, 2010; Yin et al., 2022).

Table 0.5 Binary transformations of categorical parameters in deep learning

Submergence Level [cm]				Percent Frequency Ratio		
0	-10	-15	-20	50%	70%	90%
0	0	0	1	1	0	0
0	0	0	1	0	1	0
0	0	0	1	0	0	1
0	0	1	0	1	0	0
0	0	1	0	0	1	0
0	0	1	0	0	0	1
0	1	0	0	1	0	0
0	1	0	0	0	1	0
0	1	0	0	0	0	1
1	0	0	0	1	0	0
1	0	0	0	0	1	0
1	0	0	0	0	0	1

4.4.2 Model architecture and optimization

The deep-learning model was implemented using the Python-based Keras deep-learning library and optimized through the Optuna library, which employs Bayesian optimization to minimize validation loss (Yin et al., 2022). The hyperparameter optimization process systematically refined the number of denses, units per dense, dropout, and learning rates. The final architecture, shown in Figure 4.11, had nine layers containing 448, 480, 144, 144, 112, 480, 256, 224, and 384 neurons, respectively. Dropout rates of 0.25, 0.35, 0.15, 0.30, 0.10, 0.05, 0.20, 0.35, and 0.25 were applied across respective layers to prevent overfitting and enhance generalization performance.

The Swish activation function was utilized to learn complex relationships effectively during training. It outperformed conventional functions in minimizing validation loss according to the Optuna optimization (Ramachandran et al., 2017). The learning rate was optimized to 0.000251 to ensure stable learning and further reduce validation loss. An early stopping mechanism with a patience value of 12 was employed to avoid overfitting. The training stops when the validation loss ceases to improve for 12 epochs. Initially, a maximum of 80 epochs was set, with early stopping halting at epoch 38 when the validation loss ceased to improve (Hussein & Shareef, 2024; Orr & Müller, 1998).

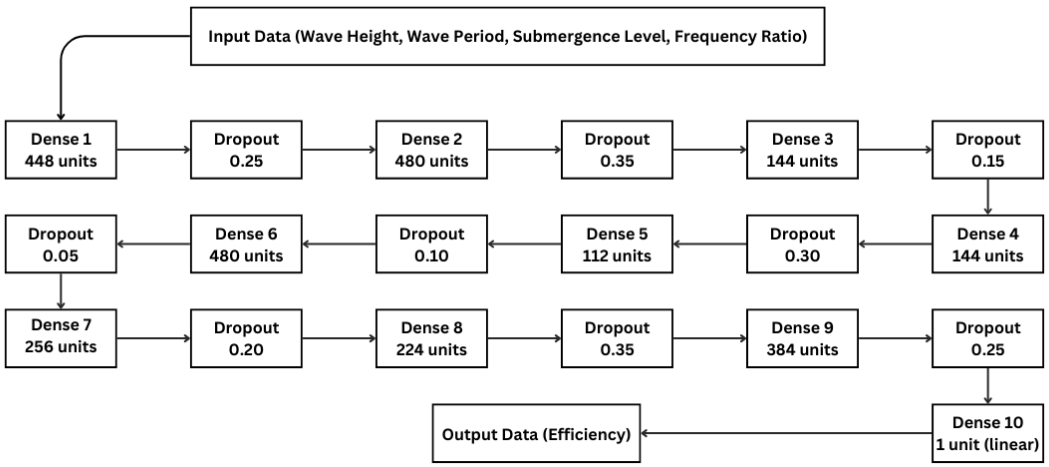

Figure 0.11 The flow diagram representation of the deep learning model

4.4.3 Model performance assessment and validation

The model's performance was monitored throughout the training iterations to prevent overfitting, as in Figure 4.12. The training/validation losses and the mean absolute errors were tracked over each epoch. As more epochs were run, the losses decreased and eventually stabilized. The alignment between training/validation losses demonstrated that overfitting was avoided, and generalization to the validation dataset was achieved at the 38th epoch. The graphs indicated low error levels on the datasets, highlighting the model's strong generalization capacity (Orr & Müller, 1998).

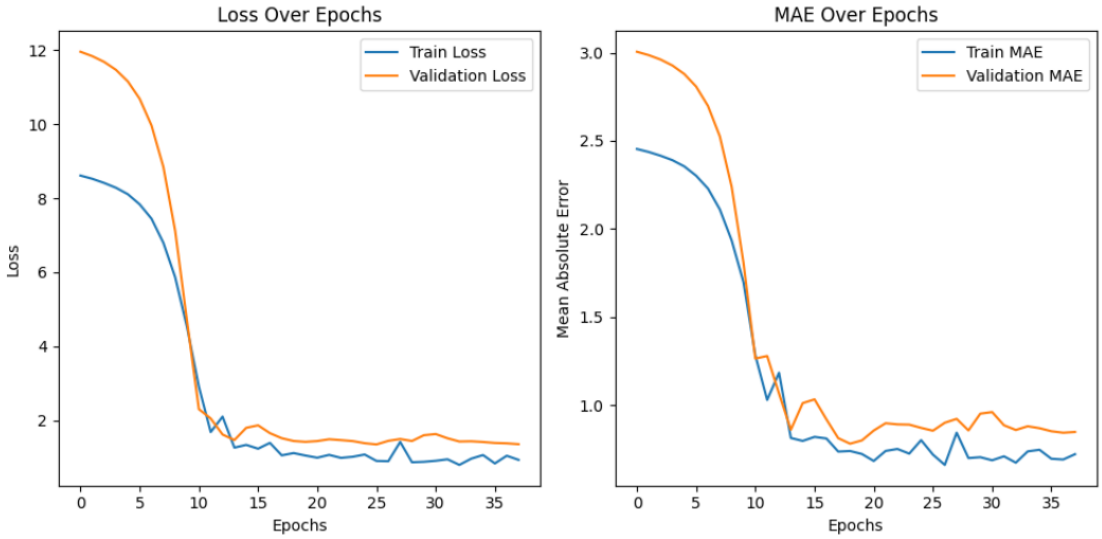

Figure 0.12 History of the training and validation losses and mean absolute error

The conversion efficiency values calculated by the model for the same operational conditions of the present study are visualized in the heat map plot below.

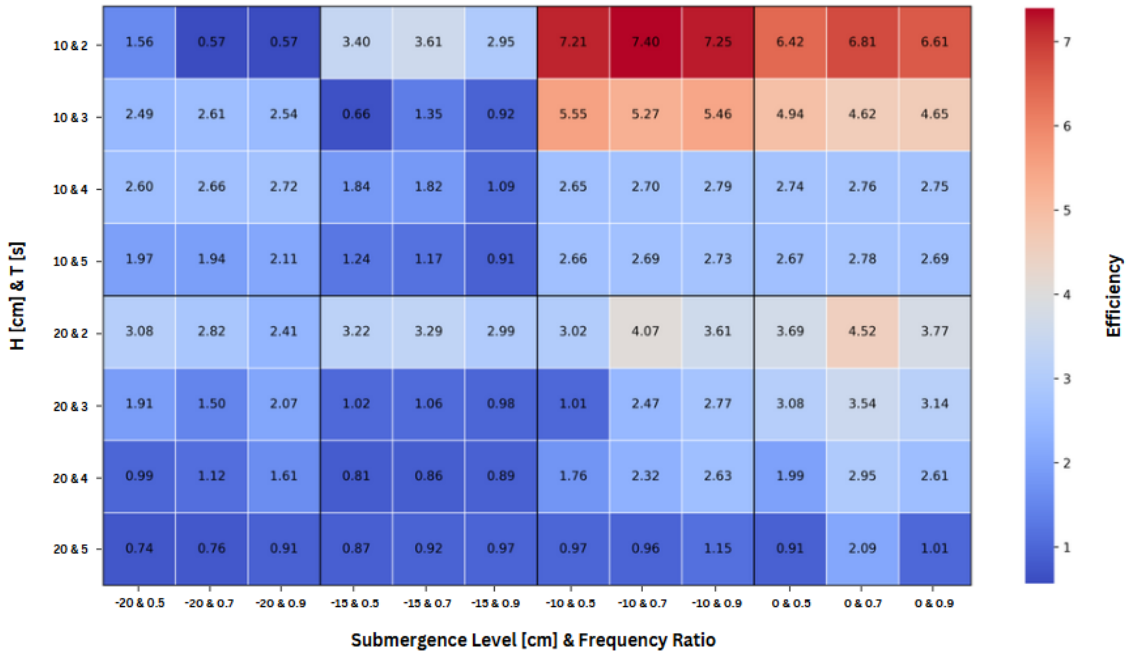

Figure 0.13 Heat map visualization of the efficiency values of the deep learning model

Multiple error metrics were used to assess the model's goodness relative to the experimental efficiency results, as indicated in Table 4.6. Finally, the offset between the model's and experimental efficiency values is shown in Figure 4.14.

Table 0.6 The error metrics used in evaluating the deep learning model

Error Metric	Value
R^2 (R-squared)	0.88
RMSE (Root Mean Squared Error)	0.55
MSE (Mean Squared Error)	0.30
MAE (Mean Absolute Error)	0.36
MAPE (Mean Absolute Percentage Error)	15.78%

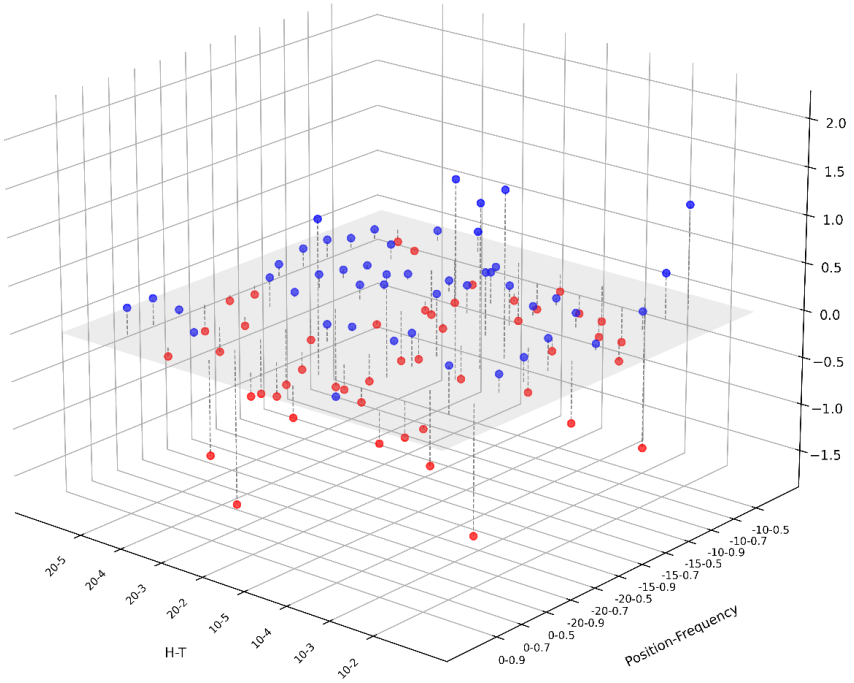

Figure 0.14 Efficiency deviation between experimental and deep learning model results

4.4.4 Feature importance and model interpretation

The Shapley Additive Explanations (SHAP) method was used to visualize the parametric influence on model-calculated efficiency results (Lundberg & Lee, 2017). The parameters included wave height, period, submergence, and frequency ratio. The results are illustrated in Figures 4.15 and 4.16. The wave period was the most influential factor in the conversion efficiency calculation. Lower wave periods and heights resulted in higher efficiencies aligning with the experimental observations. Submergence levels 0 and -10 cm contributed moderately at 15.4% and 13.5%, respectively. In contrast, the frequency ratio had a minimal impact on the model, ranging from 1.3% to 2.6%. Finally, the efficiency was seen to be mainly affected by the wave characteristics and the rotor-wave interactions, and future geometric and control optimization might enhance the performance characteristics of the prototype.

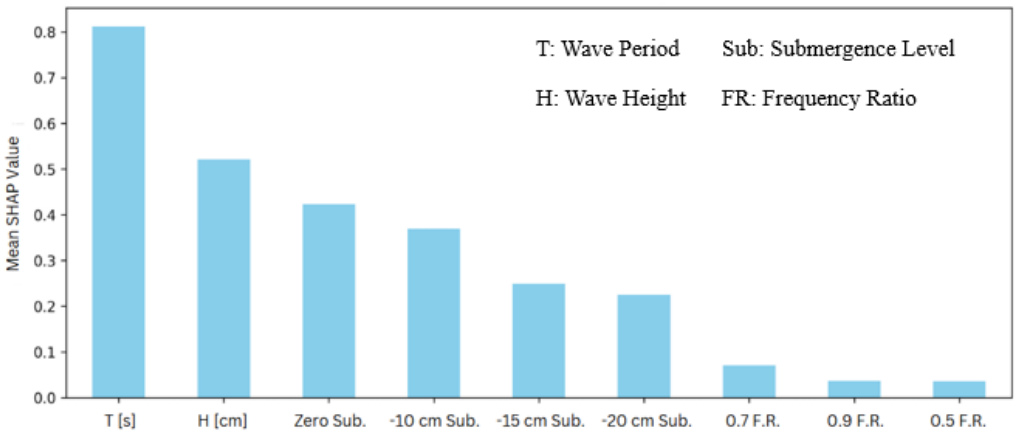

Figure 0.15 The mean SHAP values of the various operational input parameters

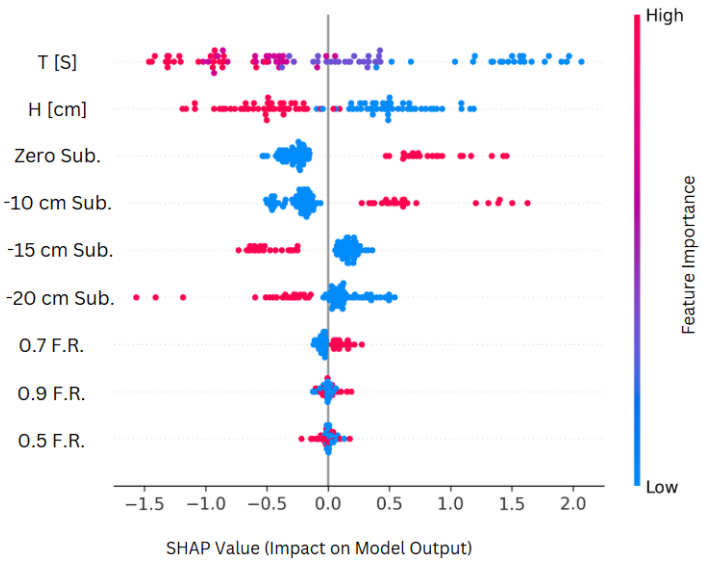

Figure 0.16 Beeswarm plot indicating the feature importance of each parameter

Figure 4.16 emphasizes the importance of optimizing the converter relative to the wave period and height conditions, which were determined to be the most critical parameters affecting efficiency, demonstrating that smaller wave periods and heights improved performance. Furthermore, the results showed that placing the rotor at the zero-submergence level or 10 cm below the free surface, at most, dramatically enhanced the conversion performance relative to further submergence. Finally, the rotational speed was deemed indifferent in terms of performance expectations.

5. CONCLUSION AND SUGGESTIONS

The conversion performance of the novel converter was experimentally investigated within a controlled wave flume at multiple regular wave and operational conditions. The converter achieved maximum efficiency (8.31%) under a submergence level of -10 cm, a wave height and period of 10 cm and 2 s, respectively, at a rotational speed corresponding to 50% of the wave's angular frequency. The efficiency values were calculated using the fifth-order nonlinear wave power results, which were compared to a rough rotor-free numerical wave flume model and linear theory.

The experimental results demonstrated improved efficiency with shorter wave periods and shallower submergence levels. However, the observed decline in efficiency with increasing wave height suggested possible instabilities in the wave-rotor interaction at the current scale, even though the theoretical energy flux was higher. A deep learning model was developed, which determined that wave period was the most significant factor affecting efficiency.

Future research should focus on larger-scale prototypes with rotor diameters comparable to wave heights at actual sea conditions to address the scaling effects of the limited wave flume dimensions, which likely influenced the observed performance. Wave-induced forces on the hydrofoils must be examined using numerical simulations and/or flow visualization techniques to optimize the design further. Performance could also be enhanced by employing more sophisticated synchronization and control techniques.

Despite all limitations, the study effectively demonstrates the viability of the proposed converter, providing proof of its concept. Additionally, it identifies specific areas that warrant further exploration, offering a foundation for future research.

REFERENCES

Ahamed, R., McKee, K., & Howard, I. (2020). Advancements of wave Energy Converters based on Power take off (PTO) Systems: A review. *Ocean Engineering, 204*.

Ahmed, M. R., Faizal, M., & Lee, Y. (2013). Optimization of blade curvature and inter-rotor spacing of Savonius rotors for maximum wave energy extraction. Ocean Engineering, 65, 32–38.

Ahmed, M. R., Faizal, M., Prasad, K., Cho, Y., Kim, C., & Lee, Y. (2010). Exploiting the orbital motion of water particles for energy extraction from waves. Journal of Mechanical Science and Technology, 24(4), 943–949.

Akimoto, H., Tanaka, K., & Kim, Y. Y. (2014). Drag-type cross-flow water turbine for capturing energy from the orbital fluid motion in ocean wave. Renewable Energy, 76, 196–203.

Alcorn, R., Hunter, S., Signorelli, C., Obeyesekera, R., Finnigan, T., & Denniss, T. (2005). Results of the testing of the Energetech Wave Energy Plant at Port Kembla.

ANSYS Inc. (2021). ANSYS Fluent Theory Guide.

Barthelemy, E. (2004). Nonlinear shallow water theories for coastal waves. Surveys in Geophysics, 25(3–4), 315–337.

Barton, I. E. (1998). Comparison of SIMPLE- and PISO-type algorithms for transient flows. International Journal for Numerical Methods in Fluids, 26(4), 459–483.

Bikas, G., Ramesh, H., & Vijaykumar, H. (2014). Study on performance of Savonius Rotor Type Wave Energy converter used in conjunction Conventional rubble mound Breakwater. Ocean Engineering, 89, 62–68.

Cameron, L., Doherty, K., Doherty, R., Henry, A., Hoff, J. V., Kaye, D., Naylor, D., Bourdier, S., & Whittaker, T. (2010). Design of the next generation of the Oyster Wave Energy Converter. In 3rd International Conference on Ocean Energy.

Christensen, L., Friis-Madsen, E., & Kofoed, J. P. (2005). The Wave Energy Challenge: The Wave Dragon Case. In Proceedings of the POWER-GEN 2005 Europe Conference.

Connell, K. O., & Cashman, A. (2016). Development of a numerical wave tank with reduced discretization error. In International Conference on Electrical, Electronics, and Optimization Techniques.

Dean, R. G., & Dalrymple, R. A. (1991). Water wave mechanics for engineers and scientists. World Scientific Publishing Company.

Depalo, F., Wang, S., Xu, S., & Soares, C. G. (2021). Design and analysis of a mooring system for a wave energy converter. Journal of Marine Science and Engineering, 9(7), 782.

Energias de Portugal. (2021, January 25). Pelamis, world's first commercial wave energy project, Agucadoura. Power Technology.

Ermakov, A., Marie, A., & Ringwood, J. V. (2022a). Optimal control of pitch and rotational velocity for a cyclorotor wave energy device. IEEE Transactions on Sustainable Energy, 13(3), 1631–1640.

Ermakov, A., Marie, A., & Ringwood, J. V. (2022b). Some fundamental results for Cyclorotor Wave energy converters for optimum power capture. IEEE Transactions on Sustainable Energy, 13(3), 1869–1872.

Ermakov, A., & Ringwood, J. V. (2021). Rotors for Wave Energy Conversion—Practice and Possibilities. IET Renewable Power Generation, 15(14), 3091–3108.

Faizal, M., Ahmed, M. R., & Lee, Y. (2010). On utilizing the orbital motion in water waves to drive a Savonius rotor. Renewable Energy, 35, 164–169.

Falcão, A. (2000). The shoreline OWC wave power plant at the Azores. In 4th European Wave Energy Conference.

Fenton, J. D. (1985). A Fifth-Order Stokes theory for steady waves. Journal of Waterway, Port, Coastal, and Ocean Engineering, 111(2), 216–234.

Fenton, J. D. (1990). Nonlinear wave theories. In B. Le Méhauté & D. M. Hanes (Eds.), The Sea: Ocean Engineering Science (Vol. 9). Wiley.

Fenton, J. D. (1998). The Cnoidal Theory of water waves. In J. B. Herbich (Ed.), Developments in Offshore Engineering (pp. 55–100).

Fenton, J. D., & McKee, W. (1990). On calculating the lengths of water waves. Coastal Engineering, 14(6), 499–513.

Folley, M., & Lamont-Kane, P. (2021). Optimum wave regime for lift-based wave energy converters. In 14th European Wave and Tidal Energy Conference (EWTEC 2021).

Goda, Y. (1983). A unified nonlinearity parameter of water waves. Report of the Port and Harbor Research Institute, 22(3), 3–30.

Goda, Y. (2010). Random seas and design of maritime structures. In Advanced series on ocean engineering.

Han, W. (2015). ATOC5051 Introduction to Physical Oceanography: Chapter 4: Ocean Waves [Lecture Notes]. University of Colorado.

Haykin, S. S. (2010). Neural networks and learning machines.

Heath, T., Whittaker, T. J. T., & Boake, C. B. (2000). The design, construction and operation of the LIMPET Wave Energy Converter. In 4th European Wave Energy Conference.

Hedges, T. S. (1995). Regions of validity of analytical wave theories. Proceedings of the Institution of Civil Engineers - Water, Maritime and Energy, 112(2), 111–114.

Hindasageri, V., Ramesh, H., & Gaurav, A. (2012). Effect of variation of wave height and ocean depth on the performance of Savonius rotors utilizing the orbital motion of ocean waves in shallow waters. Journal of Sustainable Energy and Environment, 3, 53–57.

Hindasageri, V., Ramesh, H., & Kattimani, S. (2011). Performance of savonious rotors for utilizing the orbital motion of ocean waves in shallow waters. Journal of Sustainable Energy and Environment, 2, 117–119.

Holthuijsen, L. H. (2007). Waves in oceanic and coastal waters.

Hunt, J. N. (1979). Direct solution of wave dispersion equation. Journal of the Waterway, Port, Coastal and Ocean Division, 105(4), 457–459.

Hussein, B. M., & Shareef, S. M. (2024). An empirical study on the correlation between early stopping patience and epochs in deep learning. ITM Web of Conferences, 64, 01003.

IRENA. (2020). Innovation Outlook: Ocean Energy Technologies. International Renewable Energy Agency.

Iwagaki, Y. (1968). Hyperbolic waves and their shoaling. Coastal Engineering in Japan, 11(1), 1–12.

Jeans, T., Fagley, C., Siegel, S., & Seidel, J. (2013). Irregular deep ocean wave energy attenuation using a cycloidal wave energy converter. International Journal of Marine Energy, 1, 16–32.

Jin, S., Zheng, S., & Greaves, D. (2022). On the scalability of wave energy converters. Ocean Engineering, 243.

Khaware, A., Gupta, V., Srikanth, K., & Sharkey, P. (2018). Sensitivity analysis of non-linear steep waves using VOF method. In Tenth International Conference on Computational Fluid Dynamics.

Klopman, G. (1990). A note on integral properties of periodic gravity waves in the case of a non-zero mean eulerian velocity. Journal of Fluid Mechanics, 211, 609–615.

Koo, W. (2004). Fully nonlinear wave-body interactions by a 2D potential numerical wave tank [PhD Dissertation]. Texas A&M University.

Kyriazos, T., & Poga, M. (2024). Application of Machine learning models in Social Sciences: Managing Nonlinear Relationships. Encyclopedia, 4(4), 1790–1805.

Lamont-Kane, P., Folley, M., Frost, C., & Whittaker, T. (2021). Preliminary investigations into the hydrodynamic performance of lift-based wave energy converters. In 14th European Wave and Tidal Energy Conference (EWTEC 2021).

Le Méhauté, B. (1976). An introduction to hydrodynamics and water waves. In Springer eBooks.

Li, F., Yao, J., Chen, J., Jin, H., & Yuan, Z. (2022). Performance analysis of Savonius Hydrokinetic Turbine capturing wave energy under different operating strategies. Energy Conversion and Management, 251, 115006.

Li, F., Yao, J., Eskilsson, C., Pan, Y., Chen, J., & Ji, R. (2023). Investigations on the wave performance of Savonius Turbine operating under initial phase-locked strategy. Physics of Fluids, 35.

Lighthill, J. (1978). Waves in fluids. Cambridge University Press.

Liu, P., Liu, Y., Huang, S., Zhao, J., & Su, Y. (2018). Effects of regular waves on propulsion performance of flexible flapping foil. Applied Sciences, 8(6), 934.

López, I., Andreu, J., Ceballos, S., De Alegría, I. M., & Kortabarria, I. (2013). Review of wave energy technologies and the necessary power-equipment. Renewable & Sustainable Energy Reviews, 27, 413–434.

López-Ruiz, A., Bergillos, R. J., & Ortega-Sánchez, M. (2016). The importance of wave climate forecasting on the decision-making process for nearshore wave energy exploitation. Applied Energy, 182, 191–203.

Lundberg, S. M., & Lee, S. (2017). A unified approach to interpreting model predictions. Cornell University.

Méhauté, B. L., Divoky, D., & Lin, A. (1968). Shallow Water Waves a comparison of theories and experiments. In 11th Conference on Coastal Engineering.

Nelson, R. C. (1987). Design wave heights on very mild slopes — an experimental study.

Ocean Power Technologies. (2011, March). OPT Company Presentation [Slide show].

Olbert, G., & Abdel-Maksoud, M. (2023). High-fidelity modelling of lift-based wave energy converters in a numerical wave tank. Applied Energy, 347, 121460.

Orr, G. B., & Müller, K. (1998). Neural networks: Tricks of the trade. In Lecture notes in computer science.

Othman M. [Arabic CFD]. (2020, February 26). Wave simulation using fluent in 2D [Video]. YouTube.

Pinkster, J. A., & Hermans, A. J. (2007). A rotating wing for the generation of energy form waves. In 22nd International Workshop on Water Waves and Floating Bodies.

Prasad, D. D., Ahmed, M. R., & Lee, Y. (2018). Studies on the performance of Savonius rotors in a numerical wave tank. Ocean Engineering, 158, 29–37.

Qiao, D., Haider, R., Yan, J., Ning, D., & Li, B. (2020). Review of wave energy converter and design of mooring system. Sustainability, 12(19), 8251.

Ram, K., Narayan, S., Ahmed, M. R., Nakavulevu, P., & Lee, Y. (2014). In situ near-shore wave resource assessment in the Fiji Islands. Energy Sustainable Development/Energy for Sustainable Development, 23, 170–178.

Ramachandran, P., Zoph, B., & Le, Q., V. (2017). Searching for activation functions. Cornell University.

Rienecker, M. M., & Fenton, J. D. (1981). A Fourier approximation method for steady water waves. Journal of Fluid Mechanics, 104, 119–137.

Ringe, S. (2020). Designing of one directional wave tank [Master Thesis]. Uppsala Universitet.

Selimoglu, O. (2013). A propeller capable of performing fluid motion energy conversion (Patent No. WO2013180680). Turkish Patent and Trademark Office.

Siegel, S. G. (2018). Numerical benchmarking study of a cycloidal wave energy converter. Renewable Energy, 134, 390–405.

Siegel, S. G., Fagley, C., Römer, M., & McLaughlin, T. (2012). Experimental investigation of irregular wave cancellation using a cycloidal wave energy converter. In ASME 2012 31st International Conference on Ocean, Offshore and Arctic Engineering (Vol. 7).

Siegel, S. G., Jeans, T., & McLaughlin, T. (2010). Intermediate ocean wave termination using a cycloidal wave energy converter. In ASME 2010 29th International Conference on Ocean, Offshore and Arctic Engineering (Vol. 3).

Sobey, R. J., Goodwin, P., Thieke, R. J., & Westberg, R. J. (1987). Application of Stokes, Cnoidal, and Fourier wave theories. Journal of Waterway, Port, Coastal, and Ocean Engineering, 113(6), 565–587.

Stokes, G. G. (1847). On the theory of oscillatory waves. In Transactions of the Cambridge Philosophical Society, (Vol. 8, p. 441).

Svendsen, I. A. (2005). Introduction to nearshore hydrodynamics. In Advanced series on ocean engineering.

Tutar, M., & Erdem, C. (2013). Computational modelling of two-phase flow around a Savonius type wave energy converter in a two-dimensional numerical wave tank. In V International Conference on Computational Methods in Marine Engineering.

Tutar, M., & Veci, I. (2015). Experimental Wave flume study of Savonius-type multiple rotor arrays. Journal of Renewable and Sustainable Energy, 7(6).

Tutar, M., & Veci, I. (2016). Experimental study on performance assessment of Savonius rotor type wave energy converter in an experimental wave flume. IET Renewable Power Generation, 10(4), 541–550.

Ursell, F. (1953). The long-wave paradox in the theory of gravity waves. Mathematical Proceedings of the Cambridge Philosophical Society, 49(4), 685–694.

Windt, C., Davidson, J., & Ringwood, J. V. (2018). High-fidelity Numerical modelling of ocean wave energy systems: A review of computational fluid dynamics-based numerical wave tanks. Renewable and Sustainable Energy Reviews, 93, 610–630.

Yang, Y., Diaz, I., & Morales, M. (2018). A vertical-axis unidirectional rotor for wave energy conversion. Ocean Engineering, 160, 224–230.

Yang, Y., Jenet, F., Jimenez, D., Benavides, B., Cerda, J., & Lopez, A. (2018). Responsiveness comparison between a lift-type and drag-type rotor in waves. E3S Web of Conferences, 57, 02001.

Yin, S., Wu, Y., Shen, Y., & Rowlinson, S. (2022). Development of a classification framework for construction personnel's safety behavior based on machine learning. Buildings, 13(1), 43.

Zullah, M. A., & Lee, Y. (2013). Performance evaluation of a direct drive wave energy converter using CFD. Renewable Energy, 49, 237–241.

APPENDICES

Appendix 1 The MATLAB Code of Linear Wave Theory

```
%Linear Wave Theory - Wave Energ Flux Calculator
clear;
% Inputs
H = input('Wave Height [m]: ');
T = input('Wave Period [s]: ');
% Water depth in [m]
d = 0.6;
% Gravitational Acceleration [m/s^2]
g = 9.81;
% Initial guess for wavelength
lambda = (g*T^2)/(2*pi);
% Iteratively calculate wavelength using the linear dispersion relation
for iter = 1:1000 % Max iterations
   k = 2*pi/lambda; % Wave number
   new_lambda = (g*T^2)/(2*pi)*tanh(k*d);
   if abs(new_lambda - lambda) < 1e-6 % Convergence criterion
      break;
   end
   lambda = new_lambda;
end
% Celerity and Group velocity
c = lambda/T;
c_g = 0.5*c*(1+(2*k*d)/sinh(2*k*d));
% Energy density [J/m^2]
rho = 1000;
E = (rho*g*H^2)/8;
```

```
% Energy flux [W/m]
F = E*c_g;
% Determine characteristic depth region
depth_ratio = d / lambda;
if depth_ratio >= 0.5
    depth_region = 'Deep Water Wave';
elseif depth_ratio > 0.05 && depth_ratio < 0.5
    depth_region = 'Intermediate Water Wave';
else
    depth_region = 'Shallow Water Wave';
end
% Display results in a table
results = table(H, T, d, lambda, c, c_g, E, F, {depth_region}', 'VariableNames', {'WaveHeight', 'WavePeriod', 'WaterDepth', 'Wavelength', 'WaveCelerity', 'GroupVelocity', 'EnergyDensity', 'EnergyFlux', 'DepthRegion'});
disp(results);
```

Appendix 2 Coefficients of The Stokes Wave Theory

$$S = \operatorname{sech} kd$$

$$C_0 = \sqrt{\tanh kd}$$

$$C_2 = \sqrt{\tanh kd}\left[\frac{2 + 7S^2}{4(1 - S)^2}\right]$$

$$C_4 = \sqrt{\tanh kd}\left[\frac{4 = 32S - 116S^2 - 400S^3 - 71S^4 + 146S^5}{32(1 - S)^5}\right]$$

$$D_2 = -\frac{1}{2}\sqrt{\coth kd}$$

$$D_4 = \sqrt{\coth kd}\left[\frac{2 + 4S + S^2 + 2S^3}{8(1 - S)^3}\right]$$

$$B_{22} = \coth kd\left[\frac{1 + 2S}{2(1 - S)}\right]$$

$$B_{31} = \frac{-3(1 + 3S + 3S^2 + 2S^3)}{8(1 - S)^3}$$

$$B_{42} = \coth kd\left[\frac{6 - 26S - 182S^2 - 204S^3 - 25S^4 + 26S^5}{6(3 + 2S)(1 - S)^4}\right]$$

$$B_{44} = \coth kd\left[\frac{24 + 92S + 122S^2 + 66S^3 + 67S^4 + 34S^5}{24(3 + 2S)(1 - S)^4}\right]$$

$$B_{53} = \frac{9(132 + 17S - 2216S^2 - 5897S^3 - 6292S^4 - 2687S^5 + 194S^6 + 467S^7 + 82S^8)}{128(3 + 2S)(4 + S)(1 - S)^6}$$

$$B_{55} = \frac{5(300 + 1597S + 3176S^2 + 2949S^3 + 1188S^4 + 675S^5 + 1326S^6 + 827S^7 + 130S^8)}{384(3 + 2S)(4 + S)(1 - S)^6}$$

$$E_2 = \tanh kd\left[\frac{2 + 2S + 5S^2}{4(1 - S)^2}\right]$$

$$E_4 = \tanh kd\left[\frac{8 + 12S - 152S^2 - 308S^3 - 42S^4 + 77S^5}{32(1 - S)^5}\right]$$